ACS APPLIED ENERGY MATERIALS

www.acsaem.org Article

Heterojunction of Metal Plasmas and CoO Nanofilms for Ultraefficient Activity to Oxygen Evolution Electrocatalysts

Ning Pang, Xin Tong, Yunzhe Zheng, Yang Zhou, Qingdong Ruan, Dajun Wu, Rong Huang, Dayuan Xiong,* Shaohui Xu, Lianwei Wang,* and Paul K. Chu

Cite This: *ACS Appl. Energy Mater.* 2023, 6, 2707−2718 Read Online

ACCESS | Metrics & More | Article Recommendations | Supporting Information

ABSTRACT: Hydrogen production by electrolysis of water is expected to be one of the important technologies for sustainable clean energy production, but the sluggish kinetics of the oxygen evolution reaction (OER) hampers commercialization. The atomic layer deposition and high-energy metal plasma implantation were used to construct heterostructures of CoO with different thicknesses and multiple metals. Among them, the heterostructure constructed by cobalt oxide and Zr metal shows better oxygen evolution catalytic activity than other Ag, Ti, and Cr metals. With the increase of the number of Zr atoms and the thickness of the cobalt oxide layer, the OER activity first increased and then gradually decreased. The Zr500/12CoO metal−semiconductor heterojunction has a larger barrier height and more electron−hole pairs, which makes the metal surface more positively charged and promotes the adsorption of OH^-. Construction of metal−semiconductor heterojunctions provides insights into the design and surface−interface modification of efficient, low-cost, and durable electrodes for water splitting applications.

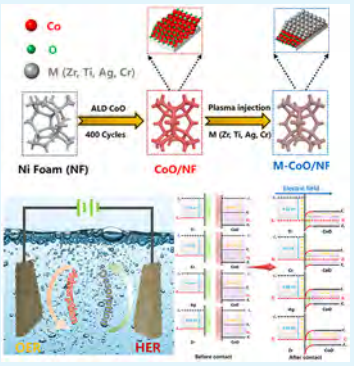

KEYWORDS: *plasma injection, atomic layer deposition, metal−semiconductor heterojunctions, surface−interface modification, oxygen evolution reaction*

1. INTRODUCTION

The demand for energy in modern life is increasing day by day, and the huge consumption of fossil fuels has brought huge environmental problems and caused long-term energy shortages.[1−3] The development of clean energy including solar energy, wind energy, and hydrogen energy is widely expected.[4,5] The hydrogen energy industry is a strategic emerging industry and a key development direction of the future industry.[6,7] Hydrogen production by electrolysis of water is an efficient, convenient, and environmentally friendly means of hydrogen production.[8,9] The electrocatalytic hydrogen production reaction is mainly divided into the following two half-reactions: hydrogen evolution reaction (HER) and oxygen evolution reaction (OER).[10] Therefore, compared with HER, the OER process involves four electrons and has disadvantages such as slow catalytic reaction kinetics, and it is particularly important to improve the catalytic activity of OER.[11−14]

At present, the catalysts used for OER on the market are mainly RuO_2 or IrO_2 related compounds.[15,16] However, their high price, difficulty in mining, and scarcity of reserves all limit their large-scale applications.[17] Transition-metal compounds are of interest due to their high efficiency, low cost, environmental friendliness, and unique physical and chemical properties for water splitting, while high-performance electrocatalysts are crucial for energy conversion devices.[18,9−20] Especially cobalt, nickel, iron, and molybdenum based materials have been comprehensively studied.[21−23] For example, Tong et al. cleverly prepared Co-doped Ni_3S_2 nanocones by vulcanizing a cobalt oxide nanofilm on the porous nickel foam (NF); the electrode exhibits excellent catalytic reactions, reaching an overpotential of 297 mV at a current density of 20 mA cm^{-2}.[24] It mainly covers oxides, sulfides, hydroxides, nitrides, and carbides of these transition metals.[25−28] Because of its unique chemical properties, variable valences, and abundant sulfur active sites, it has already demonstrated certain electrocatalytic activity in OER.[29] However, there is still room for further improvement in its oxygen evolution catalytic performance.[30]

The electrocatalytic reaction mainly focuses on the surface−interface of the catalyst; therefore, the interfacial activity is very important for the speed of the whole catalytic reaction.[31] Through the construction of heterostructures, the original active sites are activated, and the synergistic effect between the surfaces of the heterostructures jointly promotes the improvement of electrocatalytic performance.[32,33] For instance, Wang et al. ingeniously constructed a heterostructure electrode of

Received: September 15, 2022
Accepted: February 6, 2023
Published: February 27, 2023

https://doi.org/10.1021/acsaem.2c02998
ACS Appl. Energy Mater. 2023, 6, 2707−2718

carbon and spinel structure $NiCo_2O_4$, showing excellent water electrolysis performance that can drive a current density of 10 mA cm^{-2} at 1.57 V.[34] However, the research on precisely designed heterosurfaces for OER is still insufficient, and the use of atomic layer deposition (ALD) to grow cobalt oxide nanolayers and metal plasmons to form heterostructures for OER is of great significance.

Herein, we combined atomic layer deposition and high-energy metal plasma implantation to construct heterostructures of CoO with different thicknesses and multiple metals. The heterostructure constructed by 12 nm CoO and 5×10^{16} ions cm^{-2} Zr metal shows better oxygen evolution catalytic activity with low Tafel slope, overpotential (52 mV dec^{-1}, 296 mV), and excellent long-term stability. Besides, with the increase of the number of Zr atoms and the thickness of the cobalt oxide layer, the OER activity first increased and then gradually decreased. The Zr500/12CoO metal−semiconductor heterojunction has a larger barrier height and more electron−hole pairs than Ag, Cr, and Ti metals, suggesting that the metal surface is more positively charged to promote the adsorption of OH^-. The results provide insights into the design and surface−interface modification of efficient, low-cost, and durable electrodes for water splitting applications.

2. EXPERIMENTAL DETAILS

2.1. Atomic Layer Deposition of the CoO Film. The NFs (1 cm × 2 cm) were sonicated with acetone (10 mL) and 1.5 M H_2SO_4 (10 mL) for 20 min, then washed with DI water several times, and dried in a vacuum. The NF was placed in the atomic layer deposition (ALD) reaction chamber, and the ALD reaction chamber was heated to 220 °C and stabilized for 30 min. The cobalt source cobaltocene ($(\eta^5\text{-}C_5H_5)_2Co$) was maintained at a controlled temperature of 110 °C as a precursor, and N_2 was used as a carrier; another precursor, ozone (O_3 from an ozone generator), was controlled via a high-temperature pneumatic valve to generate 20 and 0.2 s pulses and then passed into the reaction chamber with a 25 s pulse. Second, purged with N_2 at a flow rate of 200 sccm, a uniform CoO film was deposited on the NF. The process was repeated for growing CoO nanofilms of different thicknesses, with a deposition rate of 0.3 Å (per cycle) due to laboratory atomic layer deposition of CoO. Therefore, the growth of 6, 9, 12, and 15 nm CoO nanofilm layers corresponds to 200, 300, 400, and 500 ALD cycles, respectively. These samples with different thicknesses were named 6 nm CoO/NF, 9 nm CoO/NF, 12 nm CoO/NF, and 15 nm CoO/NF, respectively. To further illustrate the properties of Zr, comparative samples of ZrO_2 combined with nickel foam were prepared by coating NF with commercial ZrO_2 powder and nafion solution in a 10:1 ratio, called ZrO_2/NF.

2.2. . Construction of Metal Plasmas and CoO Film Heterostructure. The samples with four thicknesses of CoO were placed in a high-energy metal plasma implantation system to coat the samples with metal plasma. The schematic diagram of the metal plasma implantation system is shown in Figure S1. Under the condition that the factors such as vacuum degree and accelerating voltage are all the same, four kinds of metal plasmas of Ag, Zr, Ti, and Cr are used to coat the samples. The changes in the thickness of the metal layers were also achieved by varying the implanted metal doses (2.5, 5, and 10×10^{16} ions cm^{-2}). In this way, we obtained a series of electrodes with metal−cobalt oxide heterostructures, the schematic diagram of which is shown in Figure S2. Take the sample with 5×10^{16} ions cm^{-2} of Zr metal plasma covering 12 nm CoO nanofilm as an example, named Zr500/12CoO/NF; 12CoO represents a 12 nm CoO nanofilm, Zr500 represents 5×10^{16} ions cm^{-2} Zr metal plasma, other corresponding electrodes and so on. Because of the high-energy metal plasma implantation, only one side exposed to the plasma atmosphere can be clad. Therefore, the metal cladding of the CoO/NF surface is one-sided. As shown in Figure S3, the brown CoO surface turns silvery white as the metal coats.

2.3. Materials Characterization. The morphology and structural features of the electrode materials were characterized by field-emission scanning electron microscopy (FESEM, Zeiss Gemini 450, Germany), transmission electron microscopy (TEM, JEOL JEM-2010), and high-angle annular dark-field scanning transmission electron microscopy (HAADF-STEM, JEM-ARM300F). The chemical composition and elemental distribution of the electrodes were tested in energy-dispersive X-ray spectrometry (EDS) equipped with SEM and TEM. The phase composition was analyzed by X-ray diffraction (XRD, Rigaku, RINT2100, Japan) with Cu Kα radiation (λ = 1.5406 Å), and the surface valence and electron transfer was analyzed by X-ray photoelectron spectroscopy (150 W, ESCALAB 250) with Al Kα radiation.

2.4. Electrochemical Measurements. Oxygen evolution reaction (OER) tests were performed at room temperature in 1 M KOH solution using a Bio-Logic workstation on various electrodes in a standard three-electrode system. The saturated calomel electrode (SCE), heterostructure catalytic electrode, and Pt sheet were used as reference electrode, working electrode, and counter electrode, respectively. Cyclic voltammetry (CV) curves were performed at 0.85−0.95 V vs RHE potential over a scan rate range of 1−200 mV s^{-1}, and linear sweep voltammetry (LSV) curves were performed at 1−2 V vs RHE potential with a sweep speed of 5 mV s^{-1}. All potentials in the LSV polarization curve are subjected to *iR* compensation, and the compensation area is based on the geometric area of the test electrode. Additionally, electrochemical impedance spectroscopy (EIS) was performed at the open circuit potential and the OER correlation potential swept from 1 MHz to 0.1 Hz. The electrochemically active area (ECSA) is obtained from the size of the electric double-layer capacitance (C_{dl}), and the C_{dl} value is obtained by CV testing in the non-Faraday region. OER stability tests were performed at a potential of 1.6 V. The potential conversion calculation formula is as follows:[22]

$$E_{RHE} = E_{SCE} + 0.0592 \times pH + 0.2415 \quad (1)$$

$$\eta_{OER} = E_{RHE} - 1.23\ V \quad (2)$$

3. RESULTS AND DISCUSSION

3.1. Fabrication and Structural Characterization. ALD technology was used to precisely grow cobalt oxide with different nanometer thicknesses (6, 9, 12, and 15 nm) and constructed metal−semiconductor-like heterostructures with different kinds of metal plasmas. The schematic diagram of the main preparation process of metal plasma/CoO heterojunction is shown in Figure 1, which is mainly divided into two steps. In the first step, the CoO with different thicknesses was grown on the surface of nickel foam (NF) by ALD. The microstructure of the 12 nm CoO/NF electrode is shown in Figure S4. The

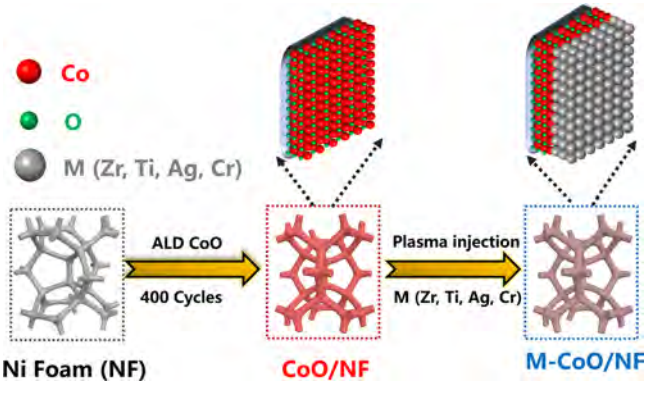

Figure 1. Schematic diagram of the construction of metal plasmonic and CoO nanofilm heterostructures.

https://doi.org/10.1021/acsaem.2c02998
ACS Appl. Energy Mater. 2023, 6, 2707−2718

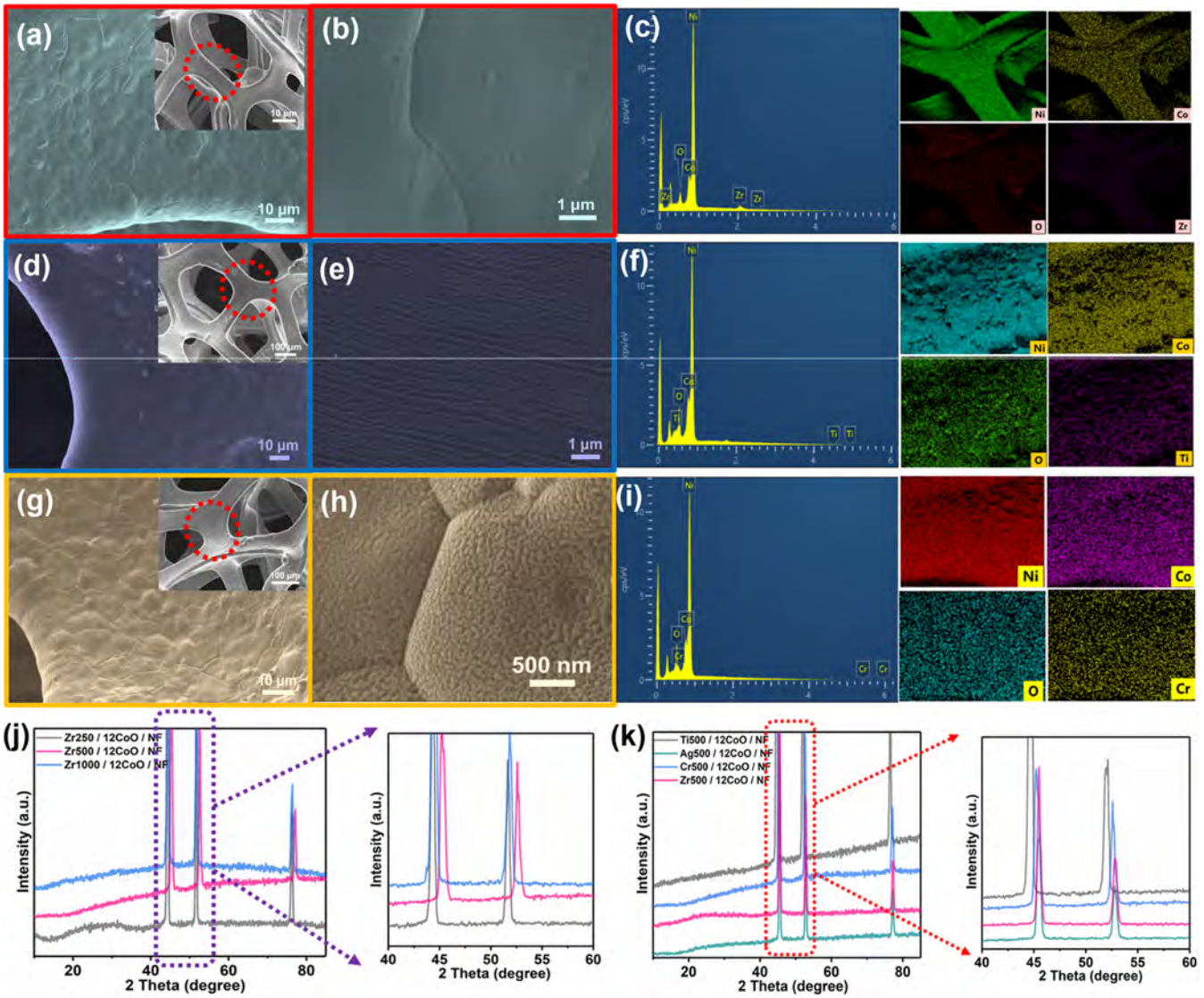

Figure 2. (a, b) SEM images of Zr500/12CoO/NF electrodes. (c) EDX and elemental maps of Zr500/12CoO/NF. (d, e) SEM images of Ti500/12CoO/NF electrodes. (f) EDX and elemental maps of Zr500/12CoO/NF. (g, h) SEM images of Cr500/12CoO/NF electrodes. (i) EDX and elemental maps of Cr500/12CoO/NF. XRD patterns: (j) Zr250/12CoO/NF, Zr500/12CoO/NF, and Zr1000/12CoO/NF; (k) Ti500/12CoO/NF, Cr500/12CoO/NF, Ag500/12CoO/NF, and Zr500/12CoO/NF.

CoO film coats the NF structure, and the surface is relatively smooth. The corresponding SEM-EDS and element distribution maps clearly exhibit that Co, Ni, and O elements are uniformly distributed on the electrode. In the second step, the metals of different types and thicknesses were coated on CoO/NF on high-energy metal plasma implantation systems. The structure, morphology, and chemical compositions of Zr500/12CoO/NF, Ti500/12CoO/NF, Cr500/12CoO/NF, and Ag500/12CoO/NF have been also investigated by SEM and EDS, and the results are given in Figures 2a–i and S10. The surfaces of Zr500/12CoO/NF and other doses of Zr plasma as well as CoO with different thicknesses electrodes in Figures 2a,b and S5–S9 are uniform and smooth. The element peaks of Ni, Co, O, and Zr are present in the EDS, and the distribution of each element is very uniform (Figure 2c). The SEM image of the Ti500/12CoO/NF, Cr500/12CoO/NF, and Ag500/12CoO/NF samples as a comparison shows that its surface is wrinkled and not smooth enough with small particles (Figures 2d–i and S10). The corresponding EDS and elemental maps display that each element is uniformly distributed on the electrode surface, demonstrating the stability of the atomic layer deposition and high-energy metal plasma implantation process.

The characterization of the lattice structure and phase of the samples is mainly using X-ray diffraction (XRD). Figures S11 and S12 show the XRD patterns of 5×10^{16} ions cm^{-2} Zr and Ti metal ions and CoO thin film heterostructure electrodes with different thicknesses (Zr500/6CoO/NF, Zr500/9CoO/NF, Zr500/12CoO/NF, Zr500/15CoO/NF, Ti500/6CoO/NF, Ti500/9CoO/NF, Ti500/12CoO/NF, and Ti500/15CoO/NF). It can be clearly seen from that the three typical Ni diffraction peaks of the entire heterostructure remain unchanged with increasing thickness of CoO and do not shift when the number of coatings is determined. However, compared with the original CoO/NF sample mentioned above, the Ni peak position is shifted to a large angle. In addition, an amorphous packet appeared at 22.5° in the entire XRD pattern, corresponding to the CoO nanofilm coated on

https://doi.org/10.1021/acsaem.2c02998
ACS Appl. Energy Mater. 2023, 6, 2707–2718

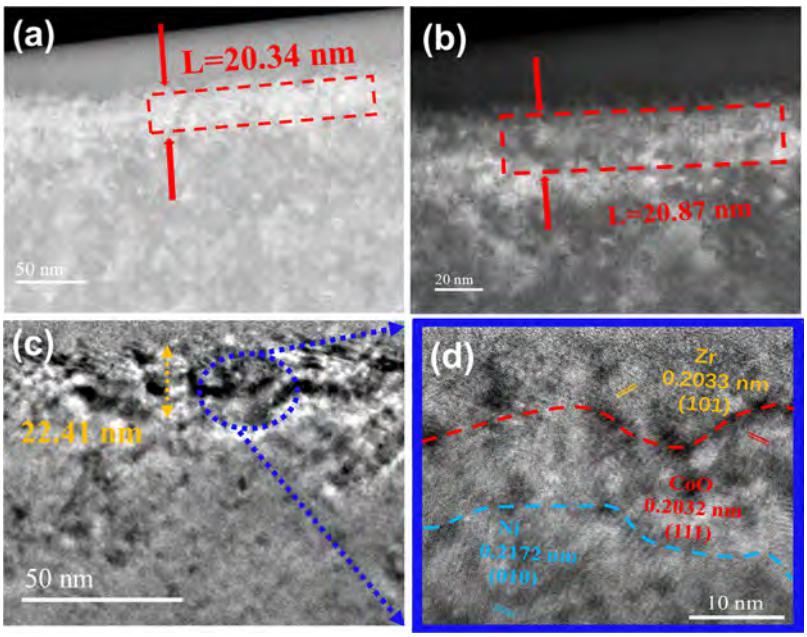

Figure 3. (a, b) HADDS-STEM images of Zr500/12CoO/NF electrodes: (a) under bright-field conditions and (b) under dark-field conditions. (c) TEM images of Zr500/12CoO/NF electrodes. (d) HR-TEM images of Zr500/12CoO/NF electrodes.

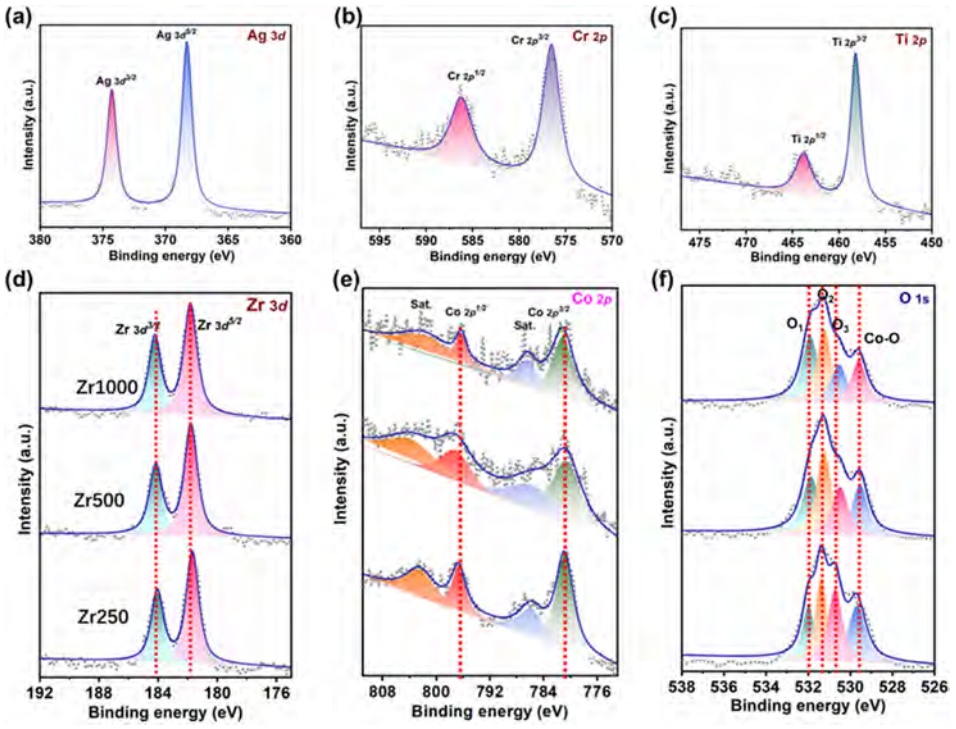

Figure 4. (a–c) Ag 3d, Cr 2p, and Ti 2p XPS spectra of Ag500/12CoO/NF, Cr500/12CoO/NF, and Ti500/12CoO/NF. (d–f) Zr 3d, Co 2p, and O 1s XPS spectra changes of Zr250/12CoO/NF, Zr500/12CoO/NF, and Zr1000/12CoO/NF.

the surface of the NF.[35] Compared with the Ni peak position of the initial CoO/NF sample, after the injection of Ti and Zr plasma, the diffraction peak shifted to the right as a whole, indicating that the lattice spacing at the interface decreased. This is mainly because the metal plasma is injected into the electrode surface with a very high energy, which releases energy in the form of squeezing the Ni lattice.[36]

To thoroughly investigate the construction of heterostructures and their related lattice spacings, particularly regarding the influence of metal plasmons containing Zr and Ag, as well as CoO nanolayers, Figures 2j and S13 display the corresponding XRD patterns. When the thickness of the cobalt oxide film remained unchanged, as the number of coated Zr and Ag metal plasmas increased from 2.5×10^{16} to 1×10^{17} ions cm^{-2}, the three typical diffraction peaks of Ni first shift to the right and then to the left, and the Ni lattice spacing at the interface first decreases and then increases. However, compared with the pristine CoO/NF samples, the lattice

https://doi.org/10.1021/acsaem.2c02998
ACS Appl. Energy Mater. 2023, 6, 2707–2718

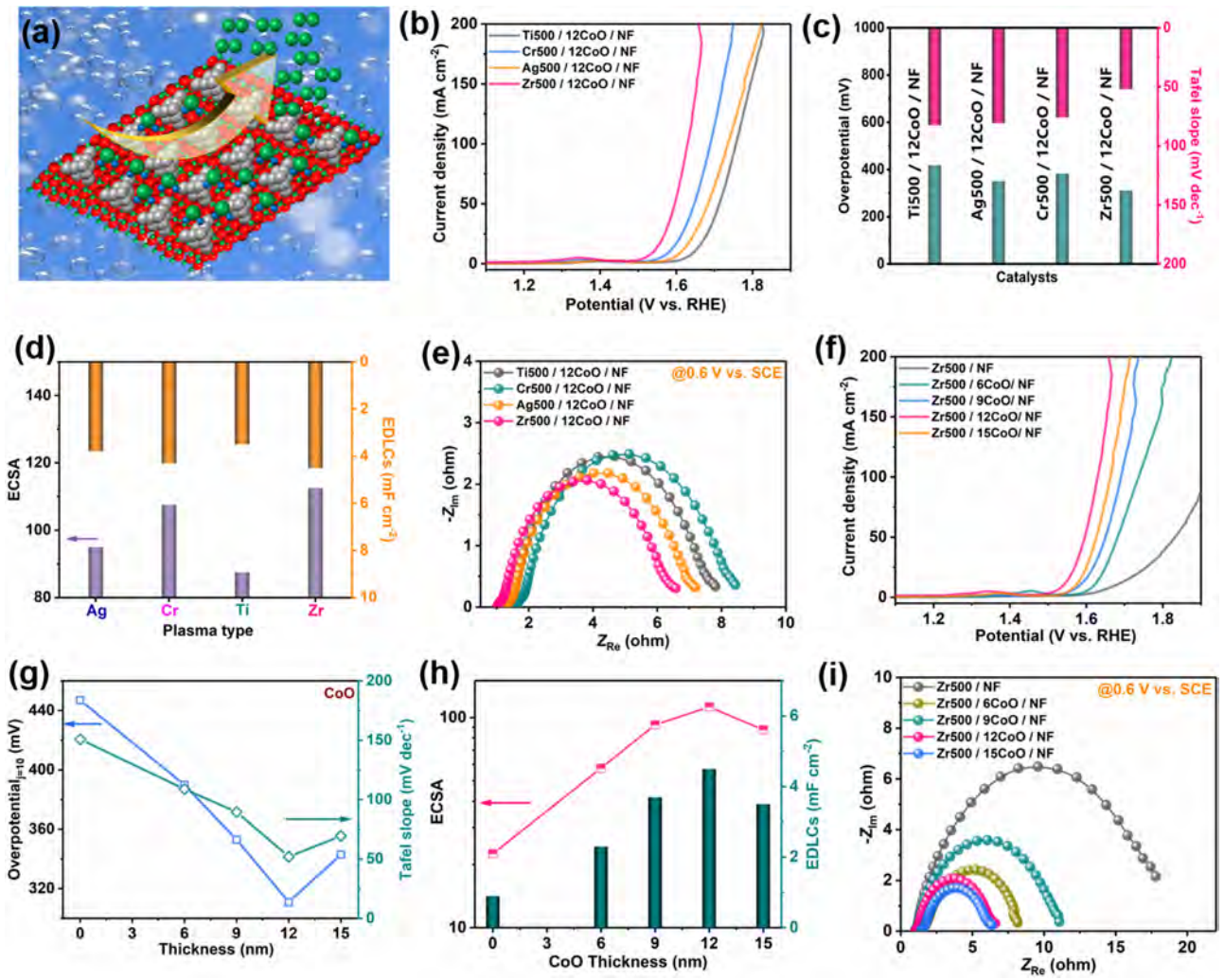

Figure 5. (a) Schematic diagram of oxygen evolution reaction of Zr500/12CoO heterojunction. Electrocatalytic activities of different catalysts. (b) Polarization curves. (c) Overpotentials and Tafel plots. (d) EDLCs and ECSA results. (e) EIS spectra obtained at 0.6 V vs RHE. Relationship between the OER activity of heterojunction and the thickness of CoO layer: (f) Corresponding LSV curves. (g) Overpotentials and Tafel plots. (h) EDLCs and ECSA results. (i) EIS spectra.

spacing of Ni coated by Zr and Ag plasma is relatively small, which may lead to a large number of distortions and defects on the surface of the heterostructure, which further promotes the OER performance of the electrode. Figure 2k shows the XRD-related diffraction peaks of Ti500/12CoO/NF, Ag500/12CoO/NF, Cr500/12CoO/NF, and Zr500/12CoO/NF. By comparison, it can be found that when the thickness of the CoO film and the number of coated metal ions are constant, the main three Ni diffraction peaks of Zr500/12CoO/NF and Ag500/12CoO/NF are more inclined to the large-angle direction compared with Ti500/12CoO/NF and Cr500/12CoO/NF. The heterostructure electrodes constructed by Ag and Zr metals have a smaller Ni lattice spacing, which may cause more distortion and defects at the surface and interface and improve the OER performance of the electrodes more greatly.

A detailed discussion of the microstructure of the electrode can make the function of the heterojunction in the catalytic reaction more explicitly. In addition, the fine morphology and lattice structure of each layer of the prepared heterojunction can be studied by HADDS-STEM and TEM. The corresponding characterization map is shown in Figure 3. The heterostructures of HADDS-STEM in bright and dark fields are shown in Figures 3a and 3b, respectively. It can clearly show that the thickness of the Zr and CoO heterojunctions is about 20 nm, which is consistent with the experimental design. In addition, the surface of the electrode is uniformly deposited on the substrate material. Above, the stability of the atomic layer deposition and high-energy metal plasma implantation process is further fully demonstrated. The composite electrode under TEM and HRTEM are characterized in Figure 3c,d. From Figure 3c, it can be seen that Zr and CoO were deposited successively on the Ni substrate to form heterojunction; the total thickness of Zr and CoO layer is about 22.41 nm. The HR-TEM of Zr/CoO/NF heterojunction (Figures 3d and S14) shows that the lattice spacing of Zr, CoO, and Ni is 0.2033, 0.2032, and 0.2017 nm, respectively, corresponding to the (101) plane of Zr, (111) plane of CoO, and (010) plane of Ni, which is consistent with XRD results. It is fully proved that the Zr and CoO structure layers grow uniformly and stably on a foam nickel substrate, respectively. In addition, as shown in the red and blue dividing lines in Figure 3d, it clearly shows the heterojunction composed of Zr, CoO, and nickel foam base.

https://doi.org/10.1021/acsaem.2c02998
ACS Appl. Energy Mater. 2023, 6, 2707−2718

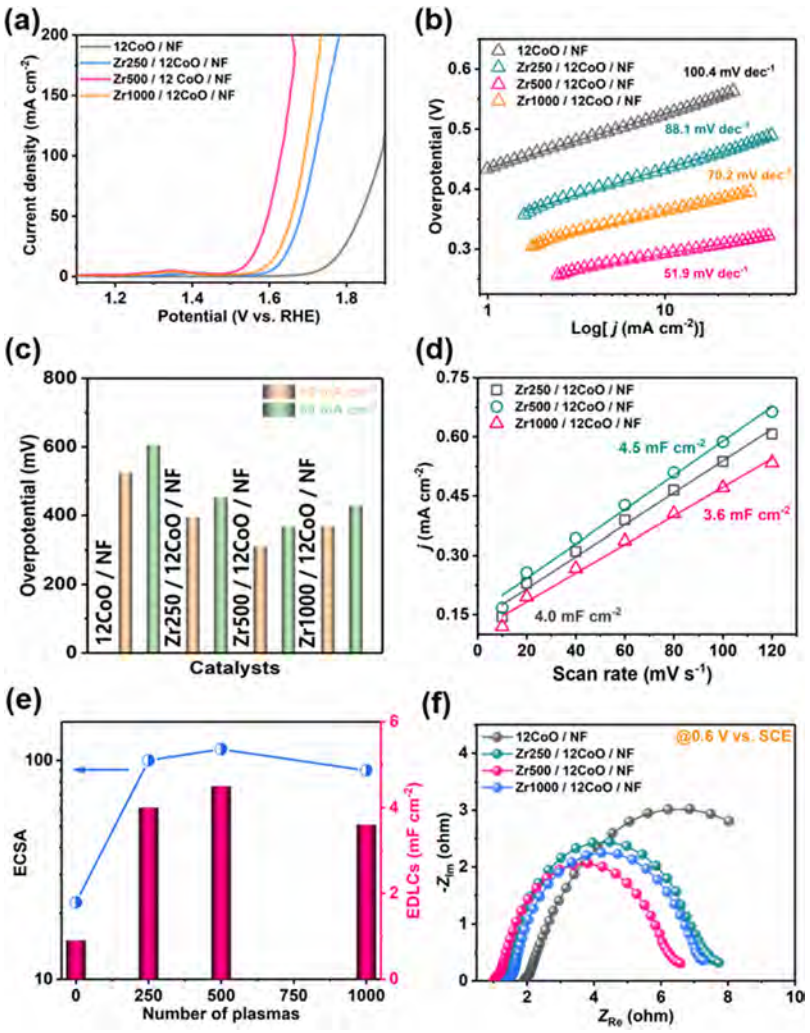

Figure 6. OER activity of different doses of Zr plasma catalysts: (a) polarization curves, (b) Tafel plots, and (c) overpotentials. (d) Plots of current density versus the speed rates. (e) EDLCs and ECSA results. (f) EIS spectra at 0.6 V vs RHE.

The chemical valence states at the electrode surface interface play a very important role in the OER process. Therefore, X-ray photoelectron spectroscopy (XPS) for Ti 2p, Cr 2p, Ag 3d, and Zr 3d was tested and analyzed in Figure 4. The Zr $3d_{3/2}$ and Zr $3d_{5/2}$ binding energy peaks corresponding to the Zr500/12CoO/NF electrode are located at 183.5 and 182 eV, respectively, and the binding energies corresponding to the Ag 3d spin−orbit in Ag500/12CoO/NF are 373.2 and 368.1 eV; these are also consistent with the reported binding energies of Ag 3d and Zr 3d (Figure 4a,d).[37,38] The binding energy peak positions of Ti $2p_{1/2}$ and Ti $2p_{3/2}$ in Ti500/12CoO/NF electrode are 463.4 and 458.3 eV, respectively, and the binding energy peak positions of Cr $2p_{1/2}$ and Cr $2p_{3/2}$ in Cr500/12CoO/NF electrode are at 586.8 and 576.1 eV, corresponding to the typical Ti 2p and Cr 2p spin−orbit energy levels, respectively (Figure 4b,c).[39,40] The Co 2p binding energies of different electrodes in Figures 4e and S15 were basically stable and did not shift. Compared with the corresponding metals, the binding energy peaks of Ti 2p, Cr 2p, Ag 3d, and Zr 3d in the Ti500/12CoO/NF, Cr500/12CoO/NF, Ag500/12CoO/NF, and Zr500/12CoO/NF electrodes are all shifted to the direction of high binding energy. Figure 4f shows the changes of O 1s XPS spectra of Zr250/12CoO/NF, Zr500/12CoO/NF, and Zr1000/12CoO/NF. The four peaks in the O 1s spectrum represent O_1 oxygen adsorption, O_2 represents O vacancy, O_3 represents water−oxygen bond, and O_4 represents Co−O oxide. The O 1s binding energy peaks in these electrodes are shifted to the lower energy direction compared with pure CoO (Figures 4f and S15). Therefore, the Ti, Cr, Ag, and Zr outer layer loses electrons, while the O outer orbital gains electrons, and electrons are transferred from Ti, Cr, Ag, and Zr to the O outer layer.[41] The electrons of the metal layer are transferred into CoO, making the metal region positively charged, which further promotes the adsorption of OH^-.

3.2. Oxygen Evolution Reaction (OER). The OER process is an important part of the whole electrolyzed water. Figure 5a shows the OER schematic diagram of the Zr500/12CoO/NF electrode at the interface of Zr metal and CoO. The polarization curves of Ti500/12CoO/NF, Cr500/12CoO/NF, Ag500/12CoO/NF, and Zr500/12CoO/NF electrodes are compared in Figure 5b, and the Zr500/12CoO/NF electrode exhibits the best OER performance, far exceeding the other three electrodes. The corresponding Tafel slope and overpotential are also given in Figure 5c. The OER Tafel slope and overpotential of the Zr500/12CoO/NF electrode in Figures S16 and S17 are 52 mV dec^{-1} and 296 mV, respectively. Compared to Ti500/12CoO/NF (83 mV dec^{-1} and 412 mV), Cr500/12CoO/NF (76 mV dec^{-1} and

https://doi.org/10.1021/acsaem.2c02998
ACS Appl. Energy Mater. 2023, 6, 2707−2718

388 mV), and Ag500/12CoO/NF (81 mV dec^{-1} and 352 mV), Zr500/12CoO/NF has better OER activity, a relatively lower Tafel slope, and a lower overpotential, suggesting that Zr metal plasmons can better activate CoO nanofilms.

The electrochemically active area (ECSA) is a very important parameter to evaluate OER activity. The electrochemical active area can be judged by the electric double-layer capacitance (C_{dl}) value. The larger the electric double-layer capacitance, the larger the electrochemically active area (Figure S18).[42] The C_{dl} value of the Zr500/12CoO/NF electrode is about 4.5 mF cm^{-2} (Figure 5d), which is higher than that of the other three electrodes (Figure S19). Therefore, the Zr500/12CoO interface has a larger electrochemically active area and is about 110. Figure S20 shows the results of TOF calculation for each active site relative to RHE when the overpotential window is 0.3−0.55 V. The TOF of Zr500/12CoO/NF reaches 0.054 s^{-1} when the overpotential is 0.4 V, which verifies the high OER performance. These results all confirm that the heterostructure surface constructed by Zr metal and 12 nm CoO has more active sites. In order to explore the effect of the electron transfer rate on the catalytic reaction at the heterogeneous surface interface during the OER process, the impedance spectroscopy test results of different samples were compared at 0.6 V vs RHE potential. As shown in Figure 5e, the solution resistance (R_s) of the Zr500/12CoO/NF electrode is 0.93 Ω, which is smaller than the other three electrodes. In addition, the charge transfer resistance (R_{ct}) of the electrode is about 2.3 Ω, indicating that this electrode has a faster electron transfer rate and better conductivity at interface compared with the other three electrodes.

Figure 5f compares the OER polarization curves of heterostructure electrodes composed of Zr metal and CoO with different thicknesse and evaluates the effect of the thickness of CoO nanolayers in the heterosurface on the OER. The OER performance of Zr500/NF electrode is far worse than other Zr metal and CoO heterostructure electrodes, which proves that the OER activity is not derived from Zr metal and NF alone. The OER performance of Zr500/12CoO/NF electrode is the best, and as the thickness of CoO increases from 0 to 15 nm, the OER performance first increases and then decreases. The related overpotential and Tafel slope are shown in Figures 5g and S21−S23. When the number of coated Zr plasmas is constant, the overpotential and Tafel slope both decrease first and then increase with the thickness of CoO. The OER activity is most prominent when the cobalt oxide thickness is 12 nm. Figure 5h shows the electric double-layer capacitance (C_{dl}) and electrochemical active area (ECSA) of the related electrode materials, which also show a basically consistent trend. The EIS impedance spectra of Zr500/NF, Zr500/6CoO/NF, Zr500/9CoO/NF, Zr500/12CoO/NF, and Zr500/15CoO/NF electrodes are shown in Figures 5i and S24. Among them, the R_s and R_{ct} of the Zr500/12CoO/NF and Zr500/15CoO/NF electrodes are much smaller than those of the other electrodes, which confirms that the Zr500/15CoO/NF electrodes have higher electrical conductivity and faster electron transport speed for the occurrence of electrocatalytic OER.

After evaluating the effect of different CoO thicknesses on the OER performance in the heterostructure, the experimental results show that another important component of the heterostructure, the Zr plasmon, also plays an important role in the OER activity. The OER polarization curves of 12CoO/NF, Zr250/12CoO/NF, Zr500/12CoO/NF, and Zr1000/12CoO/NF electrodes are depicted in Figure 6a. The OER performance of the 12CoO/NF electrode is relatively poor, much lower than that of other electrodes with heterostructures composed of Zr metal and CoO, which proves that the OER activity originates from the heterojunction composed of Zr metal and CoO. The corresponding Tafel slopes and overpotentials of these electrodes are shown in Figure 6b,c. The Tafel slope of the Zr500/12CoO/NF electrode is 51.9 mV dec^{-1}, Zr250/12CoO/NF is 88.1 mV dec^{-1}, and Zr1000/12CoO/NF is 70.2 mV dec^{-1}. The overpotentials of the Zr500/12CoO/NF electrode at current densities of 10 and 50 mA cm^{-2} are 296 and 352 mV, respectively, which are also lower than those of the other electrodes, indicating that the Zr500/12CoO/NF electrode has an optimum OER activity.

In order to understand the activation effect of catalytic activity of the Zr−CoO heterojunction in oxygen evolution reaction, the mechanism was explored. Related reaction steps are provided in the Supporting Information. First, the intermediate state containing oxygen, OH*, is negatively charged, while the metallic Zr is positively charged after semicontact with gold and can adsorb OH* to form (Zr−CoO)O*, which promotes the reaction. Similarly, the adsorption process of O*, OOH*, and OO* is continued step by step, and finally O_2 is precipitated. The increase first and then decrease trend of OER activity with the thickness of CoO and Zr layers can be ascribed to the changes occurred at the OER-active heterointerface. In the beginning, the increased Zr dose and CoO thickness can enlarge the interface area of Zr−CoO heterojunction, thus facilitating the charge transfer and thus OER. When the thickness of CoO film increases to a certain level (12 nm), the band positions can be modified and lead to less favored hole transfer from CoO to Zr (Materials Today Energy 21 (2021) 100829). On the other hand, when Zr dose increases to deeply dope into the CoO layer, the positively charged Zr in contact with CoO can be buried by the top layer of noncharged Zr (that is not in contact with CoO). In other words, the active heterojunction can be veiled by the overthick Zr layers upon high Zr doses and decrease the OER activity. All in all, the optimal coverage of CoO by Zr layer can maximally expose the heterointerface of Zr−CoO for the most active OER.

The origin of the excellent OER performance of the Zr500/12CoO/NF electrodes is the focus, and Figure 6d,e shows the magnitude of the electrochemically active area (ECSA) and electric double-layer capacitance (C_{dl}) of these electrodes as a function of the number of Zr plasmas. Figure 6d exhibits that the Zr500/12CoO/NF electrode has a C_{dl} value of 4.5 mF cm^{-2}, which is larger than those of the other two electrodes. With the increase of the number of coated Zr metal plasmas, the C_{dl} and ECSA values both show a trend of sharply increasing first and then slowly decreasing. In order to further explore the effect of the electron transport rate of the electrode on the OER performance of the electrode, the EIS impedance spectra of the 12CoO/NF, Zr250/12CoO/NF, Zr500/12CoO/NF, and Zr1000/12CoO/NF electrodes were studied (Figure 6f). The Zr500/12CoO/NF heterocatalyst has smaller solution resistance and charge transfer resistance, implying a faster electron transfer rate in OER.

To further illustrate the properties of Zr, foam nickel was coated with a 10:1 ratio of commercial ZrO_2 powder and nafion solution, named ZrO_2/NF. The XPS and XRD images of the samples are presentedn in Figure S26a, where Figure S26a displays the XRD pattern of ZrO_2/NF. The peaks of 44.5,

https://doi.org/10.1021/acsaem.2c02998
ACS Appl. Energy Mater. 2023, 6, 2707−2718

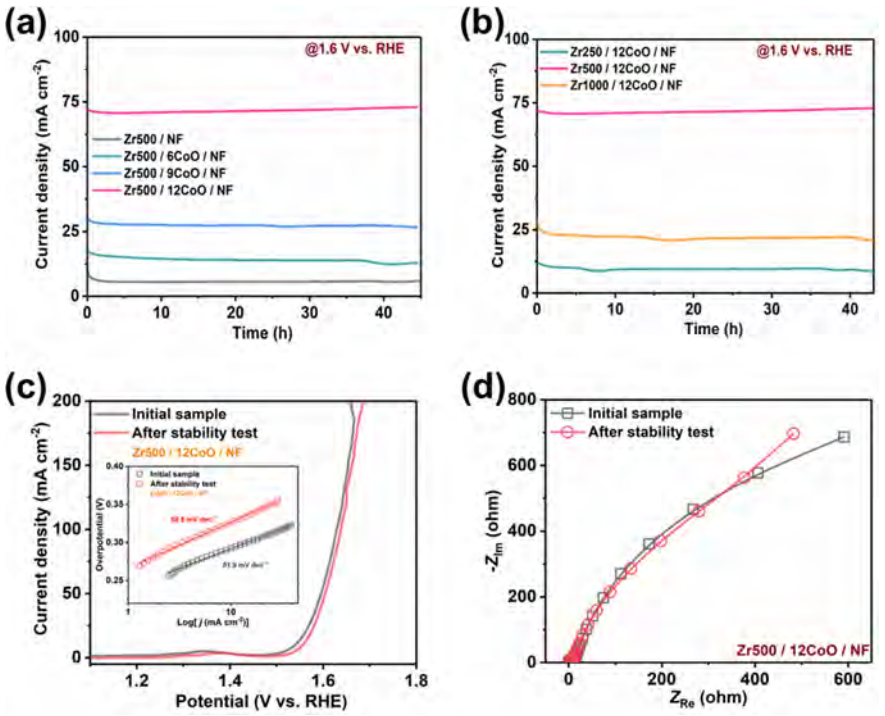

Figure 7. Long-term stability tests: (a) Zr500/6CoO/NF, Zr500/9CoO/NF, Zr500/12CoO/NF, and Zr500/15CoO/NF. (b) Zr250/12CoO/NF, Zr500/12CoO/NF, and Zr1000/12CoO/NF. (c) LSV curves of Zr500/12CoO/NF before and after stability tests. (d) EIS spectra changes before and after stability tests.

51.8, and 76.4 correspond to the (111), (200), and (220) crystal planes of Ni, respectively, while the peaks of 28.2, 31.5, 49.3, and 50.1 correspond to the (−111), (111), (022), and (220) crystal plane of ZrO_2. The binding energy peaks of $3d_{3/2}$ and Zr $3d_{5/2}$ correspond to the Zr500/12CoO/NF electrodes at 183.5 and 182 eV, respectively. The four peaks in the O 1s spectrum represent the O_1 oxygen adsorption, and O_2 represents the O vacancy. O_3 stands for the water−oxygen bond and O_4 for Co−O oxide. (Figure S26b,c). The above analysis successfully proved that ZrO_2 grows on NF.

The OER polarization curves of 12CoO/NF, ZrO_2/NF, Zr500/NF, and Zr500/12CoO/NF electrodes are depicted in Figure S27. The OER performance of the ZrO_2/NF electrode is relatively poor, much lower than Zr500/12CoO/NF, which proves that the OER activity originates from the heterojunction composed of Zr metal and CoO rather than from the oxide of Zr. The corresponding Tafel slopes and overpotentials of these electrodes are shown in Figure S27b,c. The Tafel slope of the ZrO_2/NF electrode is 58.6 mV dec^{-1}, Zr500/12CoO/NF is 51.9 mV dec^{-1}, Zr500/NF is 150.8 mV dec^{-1}, and 12CoO/NF is 100.4 mV dec^{-1}. The overpotentials of the ZrO_2/NF electrode at current densities of 10 and 50 mA cm^{-2} are 441 and 602 mV, respectively, which are also lower than those of the other Zr electrodes, indicating that Zr and CoO heterojunction electrode has an optimum OER activity. Figure S27d,e shows the magnitude of the ECSA and Cdl as a function of the four electrodes. Figure 6d exhibits that the ZrO_2/NF electrode has a C_{dl} value of 1.77 mF cm^{-2}, which is smaller than those of the other electrodes. In order to further explore the effect of the electron transport rate of the electrode on the OER performance of the electrode, the EIS impedance spectra of the 12CoO/NF, ZrO_2/NF, Zr500/NF, and Zr500/12CoO/NF electrodes were studied (Figure S23f). The ZrO_2/NF catalyst has a large solution resistance and charge transfer resistance, which means that the electron transfer rate in OER is relatively slow.

The long-term stability test of the electrode is also very necessary, which represents the durability of the electrode. As shown in Figure 7a, as the thickness of the cobalt oxide nanolayer increases, the stability increases accordingly. After the 45 h stability test of the Zr500/12CoO/NF electrode, its current density is still comparable to the initial current density, with little attenuation. Figure 7b depicts the change in stability with the increase in the number of Zr metal plasmas, which basically agrees that the greater the number of Zr metal plasmas, the better the stability. Figure 7c shows the comparison between the polarization curve and the initial polarization curve of the Zr500/12CoO/NF electrode after long-term stability test. It can be seen that the current density and Tafel slope of the polarization curve are slightly reduced, which is related to the corrosion of the electrode by the electrolyte. Similarly, the impedance spectra of the samples before and after the stability test were compared (Figure 7d), and it was observed that the impedances were basically the same, indicating that the Zr500/12CoO/NF electrode had excellent durability. The nanostructure and element distribution of the samples after the stability test are shown in Figure S25. Fine nanosheets are grown on the electrode surface, and the distribution of each element is still uniform, echoing the results of stability testing.

In order to explore the final morphology of catalyst after reaction, the catalyzed samples were characterized by XRD and XPS, as shown in Figure S28. Figure S28a shows the XRD pattern of Zr500/12CoO/NF electrode before and after the reaction. It can be clearly seen from the figure that the main peaks of the sample are basically unchanged before and after the reaction, indicating the excellent stability of the sample. Figure S28b−d shows the XPS pattern of Zr500/12CoO/NF.

https://doi.org/10.1021/acsaem.2c02998
ACS Appl. Energy Mater. 2023, 6, 2707−2718

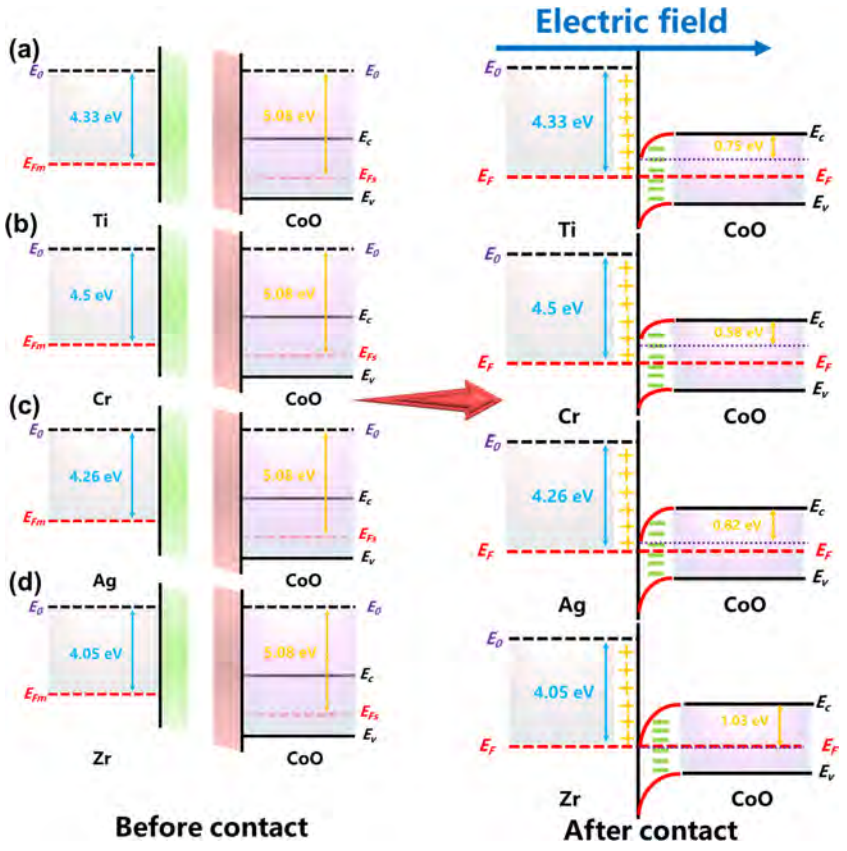

Figure 8. Work function, potential barrier, energy band, and charge transfer of CoO and metal plasma before and after contact: (a) Ti500/12CoO, (b) Cr500/12CoO, (c) Ag500/12CoO, and (d) Zr500/12CoO.

The binding energy peaks for Zr $3d_{3/2}$ and Zr $3d_{5/2}$ are at 183.5 and 182 eV, respectively. The binding energy of Co 2p is basically stable and does not shift compared to the corresponding metals. However, the peak value of O 1s binding energy basically remained unchanged, while the peak strength changed slightly, which could be attributed to the relatively small amount of CoO nanolayer growth and relatively thin thickness, so there would be slight error in the test under the coverage of Zr metal.

In order to explore the catalyst components and confirm the stability of the structure, we discussed the XPS atlas before and after the catalyst reaction (Figures 4d–f and S28b–d). By comparing the change of the binding energy peak of Zr 3d before and after the reaction, it could be attributed to the fact that the Zr metal in the Zr500/12CoO/NF sample would partially dissolve into the solution with the long-term cyclic test, and the Zr summit would appear a little shaken. However, the peak remains basically unchanged, indicating that the heterogeneous structure also remains stable, as demonstrated by the excellent performance after a long period of testing. In addition, compared with the change of O 1s, mainly with the progress of OER, the oxide generated increases, Zr is partially converted into ZrO_2, and the Zr/CoO/NF electrode will become the ZrO_2/Zr/CoO/NF electrode.

3.3. Theoretical Simulation. Based on the above analysis, it can be concluded that the metal–semiconductor heterojunctions are favorable for the boosted OER, which can be associated with the uniform heterointerface formed by plasma treatments and the positively charged metal in contact with CoO. According to previous reports on CoO-based heterojunction for OER study [*Nano Research* **2022**, *15*, 238–247], it is proposed that the main active sites should be CoO, and the doped metal facilitates the adsorption of O species (namely OH^- in the alkaline electrolyte). The oxygen evolution catalytic mechanism of metal and CoO heterojunctions is shown in Figure 8. The forbidden bandwidth of CoO is 2.6 eV. Because of the defects of Co atoms, CoO is a p-type semiconductor, so a metal–p-type semiconductor heterojunction is constructed, and the carriers are holes. Moreover, the work function W_s of CoO is 5.08 eV, while the work functions W_m of Ti, Cr, Ag, and Zr are 4.33, 4.5, 4.26, and 4.05 eV, respectively, which are all smaller than that of CoO. If the vacuum level E_0 is taken as the zero-point position, it means that the Fermi level E_{Fs} of CoO is more negative than that of the four metals (E_{Fm}). When CoO is in contact with Ti, Cr, Ag, and Zr, the holes in CoO will flow to the metal layer, leaving electrons in CoO to form a negative space charge area. The metal surface forms a positive space charge area, where the total amount of charge reaches equilibrium; the entire system remains electrically neutral.[43] After equilibrium, the metal and CoO have the same Fermi level, and no net carriers pass due to the built-in electric field, which is guided from the metal surface to the CoO body.[44] The energy band of the CoO layer loses holes, the energy band bends downward, and a potential barrier region is formed on the surface.

The OER reactivity is strongly correlated to the barrier height at the metal–semiconductor heterostructure interface.[45] The formula for the height of the barrier on the semiconductor side is as follows:[46]

$$qV_D = W_m - W_s$$

https://doi.org/10.1021/acsaem.2c02998
ACS Appl. Energy Mater. 2023, 6, 2707–2718

Therefore, it can be concluded that the barrier heights of the four metal−semiconductor heterojunctions of Ti/CoO, Cr/CoO, Ag/CoO, and Zr/CoO are 0.75, 0.58, 0.82, and 1.03 eV, respectively. The barrier height of Zr/CoO heterojunction is higher than several other heterojunctions. The formula for the Schottky barrier width is as follows:[47]

$$x_d = \left[-\frac{2\varepsilon_0\varepsilon_r(V_d + V)}{qN_D} \right]^{1/2}$$

In the formula, x_d represents the potential barrier width, ε_0 is the vacuum dielectric constant, ε_r is the relative dielectric constant, V_d represents the built-in electric field, V is the applied electric field, and N_D is the hole concentration; the direction of the applied electric field is opposite to the built-in electric field. Under other conditions being equal, the larger the built-in electric field and the larger the potential barrier width, the more holes are transferred accordingly. This result was also confirmed in XPS analysis that the binding energy of metal shifts to high binding energy while the O 1s binding energy peaks shift to lower energy compared with pure CoO (Figure 4). Therefore, the more positively charged the metal layer on the surface is, the more it can attract OH^- in the electrolyte to promote the OER. It can be clearly known that the barrier height of the Zr/CoO metal−semiconductor heterojunction is the largest compared to other samples, and the more positive charges are in the Zr metal layer, so it can stimulate the oxygen evolution, which is consistent with the experimental results.

4. CONCLUSION

In summary, heterostructures composed of four metal plasmons of Ag, Zr, Ti, and Cr with different doses and cobalt oxide nanofilms with different thicknesses were precisely constructed, exhibiting excellent OER performance in alkaline electrolytes. Compared with Ag, Ti, and Cr metal plasmas, the heterostructure electrode composed of Zr plasma with a concentration of 5×10^{16} ions cm^{-2} and 12 nm CoO nanofilm (Zr500/12CoO/NF) showed better performance. In the process of optimizing the process, when the thickness of the CoO nanofilm was determined to be 12 nm, with the increase of the Zr metal plasma implantation dose, the OER activity of the entire electrode first enhanced and then attenuated. Similarly, when the Zr plasma dose is constant, with the increase of the thickness of the CoO nanofilm, the OER performance first increases and then decreases. The metal semi-heterojunction composed of Zr metal and CoO can make holes gather on the surface of Zr metal to facilitate the adsorption of OH^- and promote the OER. This result systematically expounds the factors that affect the OER of the heterostructure between metal and cobalt oxide and lays a foundation for the subsequent design of a better metal−oxide interface to improve the electrocatalytic activity.

■ ASSOCIATED CONTENT

Supporting Information

The Supporting Information is available free of charge at https://pubs.acs.org/doi/10.1021/acsaem.2c02998.

Diagram of heterojunction structure construction process, physical image, proton transfer process; SEM correlation images of 12CoO/NF, Ag500/12CoO/NF, Zr/CoO/NF with different CoO thicknesses and different Zr atomic numbers, Zr500/12CoO/NF after stability test; XRD and XPS spectra of heterojunctions with Zr, Ti, Ag, and Cr plasma injection, ZrO_2/NF, Zr500/12CoO/NF after stability test; TOF values for OER of 12CoO/NF, Zr500/NF and Zr500/12CoO/NF; $C-V$ curves, relationship between current density and velocity, EIS measurement, Tafel slope and overpotential for Zr, Ti, Ag, Cr metal plasma-injected heterojunction; Tafel slope and overpotential for Zr/CoO/NF with different CoO thicknesses and Zr atomic numbers; OER activity of 12CoO/NF, ZrO_2/NF, Zr500/NF, and Zr500/12CoO/NF catalysts (PDF)

■ AUTHOR INFORMATION

Corresponding Authors

Lianwei Wang − *Key Laboratory of Polar Materials and Devices (MOE), Department of Electronics, East China Normal University, Shanghai 200241, P. R. China; Department of Physics, Department of Materials Science and Engineering, and Department of Biomedical Engineering, City University of Hong Kong, Kowloon, Hong Kong, China;* orcid.org/0000-0001-6368-660X; Phone: +86-021-54345160; Email: lwwang@ee.ecnu.edu.cn

Dayuan Xiong − *Key Laboratory of Polar Materials and Devices (MOE), Department of Electronics, East China Normal University, Shanghai 200241, P. R. China;* Email: dyxiong@ee.ecnu.edu.cn

Authors

Ning Pang − *Key Laboratory of Polar Materials and Devices (MOE), Department of Electronics, East China Normal University, Shanghai 200241, P. R. China*

Xin Tong − *Key Laboratory of Polar Materials and Devices (MOE), Department of Electronics, East China Normal University, Shanghai 200241, P. R. China; Jiangsu Laboratory of Advanced Functional Materials, School of Electronic and Information Engineering, Changshu Institute of Technology, Changshu 215500, China; Department of Physics, Department of Materials Science and Engineering, and Department of Biomedical Engineering, City University of Hong Kong, Kowloon, Hong Kong, China*

Yunzhe Zheng − *Key Laboratory of Polar Materials and Devices (MOE), Department of Electronics, East China Normal University, Shanghai 200241, P. R. China*

Yang Zhou − *Key Laboratory of Polar Materials and Devices (MOE), Department of Electronics, East China Normal University, Shanghai 200241, P. R. China*

Qingdong Ruan − *Department of Physics, Department of Materials Science and Engineering, and Department of Biomedical Engineering, City University of Hong Kong, Kowloon, Hong Kong, China*

Dajun Wu − *Jiangsu Laboratory of Advanced Functional Materials, School of Electronic and Information Engineering, Changshu Institute of Technology, Changshu 215500, China;* orcid.org/0000-0001-6430-380X

Rong Huang − *Key Laboratory of Polar Materials and Devices (MOE), Department of Electronics, East China Normal University, Shanghai 200241, P. R. China*

Shaohui Xu − *Key Laboratory of Polar Materials and Devices (MOE), Department of Electronics, East China Normal University, Shanghai 200241, P. R. China;* orcid.org/0000-0002-8201-0354

https://doi.org/10.1021/acsaem.2c02998
ACS Appl. Energy Mater. 2023, 6, 2707−2718

Paul K. Chu − *Department of Physics, Department of Materials Science and Engineering, and Department of Biomedical Engineering, City University of Hong Kong, Kowloon, Hong Kong, China;* orcid.org/0000-0002-5581-4883

Complete contact information is available at: https://pubs.acs.org/10.1021/acsaem.2c02998

Author Contributions

N.P. and X.T. contributed to the work equally.

Notes

The authors declare no competing financial interest.

■ ACKNOWLEDGMENTS

This work was jointly supported by National Natural Science Foundation of China (Nos. 61991444 and 61774060) and City University of Hong Kong Strategic Research Grant (SRG) (No. 7005505).

■ REFERENCES

(1) Stamenkovic, V. R.; Strmcnik, D.; Lopes, P. P.; Markovic, N. M. Energy and fuels from electrochemical interfaces. *Nat. Mater.* **2017**, *16* (1), 57−69.

(2) Grimaud, A.; Demortière, A.; Saubanère, M.; Dachraoui, W.; Duchamp, M.; Doublet, M.-L.; Tarascon, J.-M. Activation of surface oxygen sites on an iridium-based model catalyst for the oxygen evolution reaction. *Nat. Energy* **2017**, DOI: 10.1038/nenergy.2016.189.

(3) Zhao, S.; Tan, C.; He, C.-T.; An, P.; Xie, F.; Jiang, S.; Zhu, Y.; Wu, K.-H.; Zhang, B.; Li, H.; Zhang, J.; Chen, Y.; Liu, S.; Dong, J.; Tang, Z. Structural transformation of highly active metal−organic framework electrocatalysts during the oxygen evolution reaction. *Nat. Energy* **2020**, *5* (11), 881−890.

(4) Li, Z.; Zhang, W.; Zhang, R.; Sun, H. Development of renewable energy multi-energy complementary hydrogen energy system (A Case Study in China): A review. *Energy Exploration & Exploitation* **2020**, *38* (6), 2099−2127.

(5) Ding, H.; Liu, H.; Chu, W.; Wu, C.; Xie, Y. Structural Transformation of Heterogeneous Materials for Electrocatalytic Oxygen Evolution Reaction. *Chem. Rev.* **2021**, *121* (21), 13174−13212.

(6) Gao, L.; Cui, X.; Sewell, C. D.; Li, J.; Lin, Z. Recent advances in activating surface reconstruction for the high-efficiency oxygen evolution reaction. *Chem. Soc. Rev.* **2021**, *50* (15), 8428−8469.

(7) Zhao, G.; Li, P.; Cheng, N.; Dou, S. X.; Sun, W. An Ir/$Ni(OH)_2$ Heterostructured Electrocatalyst for the Oxygen Evolution Reaction: Breaking the Scaling Relation, Stabilizing Iridium(V), and Beyond. *Adv. Mater.* **2020**, *32* (24), 2000872.

(8) Zou, X.; Zhang, Y. Noble metal-free hydrogen evolution catalysts for water splitting. *Chem. Soc. Rev.* **2015**, *44* (15), 5148−5180.

(9) Jung, S. Y.; Kang, S.; Kim, K. M.; Mhin, S.; Kim, J. C.; Kim, S. J.; Enkhtuvshin, E.; Choi, S.; Han, H. Sulfur-incorporated nickel-iron layered double hydroxides for effective oxygen evolution reaction in seawater. *Appl. Surf. Sci.* **2021**, *568*, 150965.

(10) Wilhelm, M.; Bastos, A.; Neves, C.; Martins, R.; Tedim, J. Ni-Fe layered double hydroxides for oxygen evolution Reaction: Impact of Ni/Fe ratio and crystallinity. *Mater. Design* **2021**, *212*, 110188.

(11) Suen, N. T.; Hung, S. F.; Quan, Q.; Zhang, N.; Xu, Y. J.; Chen, H. M. Electrocatalysis for the oxygen evolution reaction: recent development and future perspectives. *Chem. Soc. Rev.* **2017**, *46* (2), 337−365.

(12) Chen, W.-Z.; Zhang, M.; Liu, Y.; Yao, X.-M.; Liu, P.-Y.; Liu, Z.; He, J.; Wang, Y.-Q. Super-hydrophilic MgO/$NiCo_2S_4$ heterostructure for high-efficient oxygen evolution reaction in neutral electrolytes. *Appl. Catal. B: Environ.* **2022**, *312*, 121432.

(13) Li, J. Oxygen Evolution Reaction in Energy Conversion and Storage: Design Strategies Under and Beyond the Energy Scaling Relationship. *Nanomicro Lett.* **2022**, *14* (1), 112.

(14) Li, J.; Li, J.; Ren, J.; Hong, H.; Liu, D.; Liu, L.; Wang, D. Electric-Field-Treated Ni/Co(3)O(4) Film as High-Performance Bifunctional Electrocatalysts for Efficient Overall Water Splitting. *Nanomicro Lett.* **2022**, *14* (1), 148.

(15) Chen, J.; Li, H.; Chen, S.; Fei, J.; Liu, C.; Yu, Z.; Shin, K.; Liu, Z.; Song, L.; Henkelman, G.; Wei, L.; Chen, Y. Co−Fe−Cr (oxy)Hydroxides as Efficient Oxygen Evolution Reaction Catalysts. *Adv. Energy Mater.* **2021**, *11* (11), 2003412.

(16) Hu, J.; Liang, Y. Q.; Wu, S. L.; Li, Z. Y.; Shi, C. S.; Luo, S. Y.; Sun, H. J.; Zhu, S. L.; Cui, Z. D. Hierarchical nickle-iron layered double hydroxide composite electrocatalyst for efficient oxygen evolution reaction. *Mater. Today Nano* **2022**, *17*, 100150.

(17) Chen, J.; Long, Q.; Xiao, K.; Ouyang, T.; Li, N.; Ye, S.; Liu, Z.-Q. Vertically-interlaced NiFeP/MXene electrocatalyst with tunable electronic structure for high-efficiency oxygen evolution reaction. *Sci. Bulletin* **2021**, *66* (11), 1063−1072.

(18) Tong, X.; Li, Y.; Pang, N.; Zhou, Y.; Wu, D.; Xiong, D.; Xu, S.; Wang, L.; Chu, P. K. Highly active cobalt-doped nickel sulfide porous nanocones for high-performance quasi-solid-state zinc-ion batteries. *J. Energy Chem.* **2022**, *66*, 237−249.

(19) Wu, L.; Zhang, J.; Wang, S.; Jiang, Q.; Feng, R.; Ju, S.; Zhang, W.; Song, F. Silver decorated hydroxides electrocatalysts for efficient oxygen evolution reaction. *Chem. Eng. J.* **2022**, *442*, 136168.

(20) Zeng, X.; Cai, Z.; Zhang, C.; Wang, D.; Xu, J.; Wang, X. Novel NiFe-LDH@Ni-MOF/NF heterostructured electrocatalysts for efficient oxygen evolution. *Mater. Res. Lett.* **2022**, *10* (2), 88−96.

(21) Tong, X.; Wu, D.; Zhang, C.; Lian, K.; Xiong, D.; Xu, S.; Zhu, Y.; Qi, R.; Huang, R.; Wang, L.; Chu, P. K. Three-dimensional tetsubo-like $Co(OH)_2$ nanorods on a macroporous electrically conductive network as an efficient electroactive framework for the hydrogen evolution reaction. *J. Mater. Chem. A* **2017**, *5* (6), 2629−2639.

(22) Chen, P.; Tong, Y.; Wu, C.; Xie, Y. Surface/Interfacial Engineering of Inorganic Low-Dimensional Electrode Materials for Electrocatalysis. *Acc. Chem. Res.* **2018**, *51* (11), 2857−2866.

(23) Jin, H.; Liu, X.; Chen, S.; Vasileff, A.; Li, L.; Jiao, Y.; Song, L.; Zheng, Y.; Qiao, S.-Z. Heteroatom-Doped Transition Metal Electrocatalysts for Hydrogen Evolution Reaction. *ACS Energy Lett.* **2019**, *4* (4), 805−810.

(24) Tong, X.; Li, Y.; Pang, N.; Qu, Y.; Yan, C.; Xiong, D.; Xu, S.; Wang, L.; Chu, P. K. Co-doped Ni_3S_2 porous nanocones as high-performance bifunctional electrocatalysts in water splitting. *Chem. Eng. J.* **2021**, *425*, 130455.

(25) Najafi, L.; Bellani, S.; Oropesa-Nuñez, R.; Ansaldo, A.; Prato, M.; Del Rio Castillo, A. E.; Bonaccorso, F. Engineered $MoSe_2$-Based Heterostructures for Efficient Electrochemical Hydrogen Evolution Reaction. *Adv. Energy Mater.* **2018**, *8* (16), 1703212.

(26) Yang, Y.; Lin, M.; Song, Y.; Tuerhong, G.; Dai, J.; Zhang, T.; Guo, D.; Liu, L. Interfacial microenvironment modulation enhancing catalytic kinetics of bimetallic (oxy)hydroxide heterostructures for highly efficient oxygen evolution reaction. *J. Alloys Compd.* **2022**, *910*, 164879.

(27) Li, L.; Wang, P.; Shao, Q.; Huang, X. Recent Progress in Advanced Electrocatalyst Design for Acidic Oxygen Evolution Reaction. *Adv. Mater.* **2021**, *33* (50), 2004243.

(28) Tong, X.; Li, Y.; Ruan, Q.; Pang, N.; Zhou, Y.; Wu, D.; Xiong, D.; Xu, S.; Wang, L.; Chu, P. K. Plasma Engineering of Basal Sulfur Sites on MoS_2@Ni_3S_2 Nanorods for the Alkaline Hydrogen Evolution Reaction. *Adv. Sci.* **2022**, *9*, 2104774.

(29) Hao, Y.; Du, G.; Fan, Y.; Jia, L.; Han, D.; Zhao, W.; Su, Q.; Ding, S.; Xu, B. Mo/P Dual-Doped Co/Oxygen-Deficient Co_3O_4 Core-Shell Nanorods Supported on Ni Foam for Electrochemical Overall Water Splitting. *ACS Appl. Mater. Interfaces* **2021**, *13* (46), 55263−55271.

(30) Ma, H.; Chen, Z.; Wang, Z.; Singh, C. V.; Jiang, Q. Interface Engineering of Co/CoMoN/NF Heterostructures for High-Perform-

ance Electrochemical Overall Water Splitting. *Adv. Sci. (Weinh)* **2022**, *9*, 2105313.
(31) Zhang, H.; Hagen, D. J.; Li, X.; Graff, A.; Heyroth, F.; Fuhrmann, B.; Kostanovskiy, I.; Schweizer, S. L.; Caddeo, F.; Maijenburg, A. W.; Parkin, S.; Wehrspohn, R. B. Atomic Layer Deposition of Cobalt Phosphide for Efficient Water Splitting. *Angew. Chem., Int. Ed. Engl.* **2020**, *59* (39), 17172−17176.
(32) Wang, C.; Zhai, P.; Xia, M.; Wu, Y.; Zhang, B.; Li, Z.; Ran, L.; Gao, J.; Zhang, X.; Fan, Z.; Sun, L.; Hou, J. Engineering Lattice Oxygen Activation of Iridium Clusters Stabilized on Amorphous Bimetal Borides Array for Oxygen Evolution Reaction. *Angew. Chem., Int. Ed. Engl.* **2021**, *60* (52), 27126−27134.
(33) Yu, M.; Budiyanto, E.; Tuysuz, H. Principles of Water Electrolysis and Recent Progress in Cobalt-, Nickel-, and Iron-Based Oxides for the Oxygen Evolution Reaction. *Angew. Chem., Int. Ed. Engl.* **2022**, *61* (1), 202103824.
(34) Ai, L.; Wang, Y.; Luo, Y.; Tian, Y.; Yang, S.; Chen, M.; Jiang, J. Robust interfacial Ru-RuO_2 heterostructures for highly efficient and ultrastable oxygen evolution reaction and overall water splitting in acidic media. *J. Alloys Compd.* **2022**, *902*, 163787.
(35) Xiong, Y.; Xu, L.; Jin, C.; Sun, Q. Interface-engineered atomically thin Ni_3S_2/MnO_2 heterogeneous nanoarrays for efficient overall water splitting in alkaline media. *Appl. Catal. B: Environ.* **2019**, *254*, 329−338.
(36) Zhao, J. W.; Shi, Z. X.; Li, C. F.; Gu, L. F.; Li, G. R. Boosting the electrocatalytic performance of NiFe layered double hydroxides for the oxygen evolution reaction by exposing the highly active edge plane (012). *Chem. Sci.* **2021**, *12* (2), 650−659.
(37) Xu, Y.; Cheng, Z.; Jiang, J.; Du, J.; Xu, Q. 2D amorphous bi-metallic NiFe nitrides for a high-efficiency oxygen evolution reaction. *Chem. Commun. (Camb)* **2021**, *57* (97), 13170−13173.
(38) Yang, K.; Jin, Z.; Zhang, Q.; Chen, Q.; Peng, W.; Li, Y.; Zhang, F.; Xia, Q.; Fan, X. Reconstruction of bimetal $CoFe_{0.13}$-MOF to enhance the catalytic performance in the oxygen evolution reaction. *Chem. Commun. (Camb)* **2022**, *58* (8), 1115−1118.
(39) Ren, J.; Zheng, L.; Su, Y.; Meng, P.; Zhou, Q.; Zeng, H.; Zhang, T.; Yu, H. Competitive adsorption of Cd(II), Pb(II) and Cu(II) ions from acid mine drainage with zero-valent iron/phosphoric titanium dioxide: XPS qualitative analyses and DFT quantitative calculations. *Chem. Eng. J.* **2022**, *445*, 136778.
(40) Shen, T. H.; Spillane, L.; Vavra, J.; Pham, T. H. M.; Peng, J.; Shao-Horn, Y.; Tileli, V. Oxygen Evolution Reaction in $Ba_{0.5}Sr_{0.5}Co_{0.8}Fe_{0.2}O_3$-delta Aided by Intrinsic Co/Fe Spinel-Like Surface. *J. Am. Chem. Soc.* **2020**, *142* (37), 15876−15883.
(41) Tong, X.; Li, Y.; Ruan, Q.; Pang, N.; Zhou, Y.; Wu, D.; Xiong, D.; Xu, S.; Wang, L.; Chu, P. K. Plasma Engineering of Basal Sulfur Sites on MoS2 @Ni3 S2 Nanorods for the Alkaline Hydrogen Evolution Reaction. *Adv. Sci.* **2022**, *9* (6), 2104774.
(42) Li, G. F.; Divinagracia, M.; Labata, M. F.; Ocon, J. D.; Abel Chuang, P. Y. Electrolyte-Dependent Oxygen Evolution Reactions in Alkaline Media: Electrical Double Layer and Interfacial Interactions. *ACS Appl. Mater. Interfaces* **2019**, *11* (37), 33748−33758.
(43) Liang, Z.; Zhou, W.; Gao, S.; Zhao, R.; Zhang, H.; Tang, Y.; Cheng, J.; Qiu, T.; Zhu, B.; Qu, C.; Guo, W.; Wang, Q.; Zou, R. Fabrication of Hollow CoP/TiOx Heterostructures for Enhanced Oxygen Evolution Reaction. *Small* **2020**, *16* (2), 1905075.
(44) Jiao, J.; Yang, W.; Pan, Y.; Zhang, C.; Liu, S.; Chen, C.; Wang, D. Interface Engineering of Partially Phosphidated Co@Co-P@ NPCNTs for Highly Enhanced Electrochemical Overall Water Splitting. *Small* **2020**, *16* (41), 2002124.
(45) Liu, Y.; Gu, X.; Qi, W.; Zhu, H.; Shan, H.; Chen, W.; Tao, P.; Song, C.; Shang, W.; Deng, T.; Wu, J. Enhancing the Photocatalytic Hydrogen Evolution Performance of a Metal/Semiconductor Catalyst through Modulation of the Schottky Barrier Height by Controlling the Orientation of the Interface. *ACS Appl. Mater. Interfaces* **2017**, *9* (14), 12494−12500.
(46) Xu, X.; He, Y.; Huang, W.; Cao, A.; Kang, L.; Liu, J. Heterostructure of Semiconductors on Self-Supported Cuprous Phosphide Nanowires for Enhanced Overall Water Splitting. *ACS Appl. Mater. Interfaces* **2022**, *14* (15), 17520−17530.
(47) Lou, P.; Lee, J. Y. GeC/GaN vdW Heterojunctions: A Promising Photocatalyst for Overall Water Splitting and Solar Energy Conversion. *ACS Appl. Mater. Interfaces* **2020**, *12* (12), 14289−14297.

https://doi.org/10.1021/acsaem.2c02998
ACS Appl. Energy Mater. 2023, 6, 2707−2718

Supporting Information

Heterojunction of metal plasmas and CoO nanofilms for ultra-efficient activity to oxygen evolution electrocatalysts

Ning Pang[a†], Xin Tong[a, b, c†], Yunzhe Zheng[a], Yang Zhou[a], Qingdong Ruan[c], Dajun Wu[b], Rong Huang[a], Dayuan Xiong[a*], Shaohui Xu[a], Lianwei Wang[a, c*], Paul K. Chu[c]

[a] *Key Laboratory of Polar Materials and Devices (MOE), Department of Electronics, East China Normal University, 500 Dongchuan Road, Shanghai 200241, P. R. China*

[b] *Jiangsu Laboratory of Advanced Functional Materials, School of Electronic and Information Engineering, Changshu Institute of Technology, Changshu 215500, China*

[c] *Department of Physics, Department of Materials Science and Engineering, and Department of Biomedical Engineering, City University of Hong Kong, Tat Chee Avenue, Kowloon, Hong Kong, China*

Corresponding Authors:

***** L.W. Wang (Tel: +86-021-54345160; Email: lwwang@ee.ecnu.edu.cn); D.Y. Xiong (Email: dyxiong@ee.ecnu.edu.cn)

[†]These two authors contributed to the work equally.

Proton-transfer process

OER involves multiple proton-transfer processes as shown in **S1**-**S5**:

S1: $S + OH^- \rightarrow SOH^* + e^-$

S2: $SOH^* + OH^- \rightarrow SO^* + H_2O + e^-$

S3: $SO^* + OH^- \rightarrow SOOH^* + e^-$

S4: $SOOH^* + OH^- \rightarrow SOO^* + H_2O + e^-$

S5: $SOO^* \rightarrow S + O_2$.

Here, S represents the active site (Zr-CoO) when OER occurs and SOH^*, SO^*, $SOOH^*$ are the intermediate species adsorbed on the active sites.

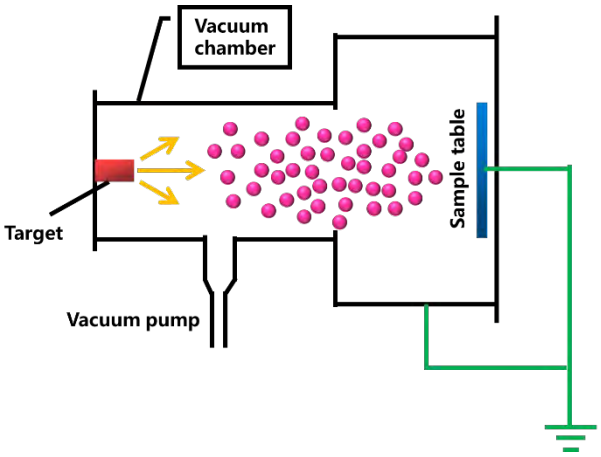

Figure S1. Schematic diagram of the high-energy metal plasma implantation system.

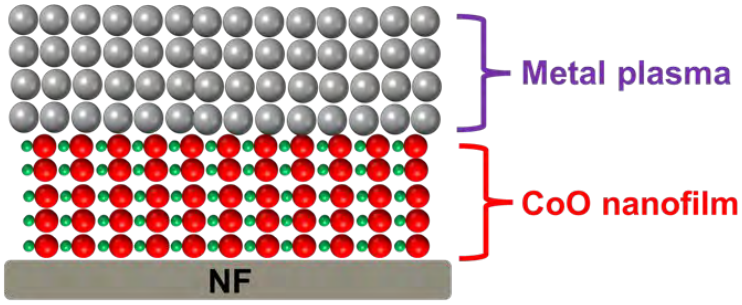

Figure S2. Schematic illustration of the heterostructure constructed by CoO nanofilms and metal plasmons.

Figure S3. Physical images of NF, 12 nm CoO/NF, and M-12CoO/NF samples.

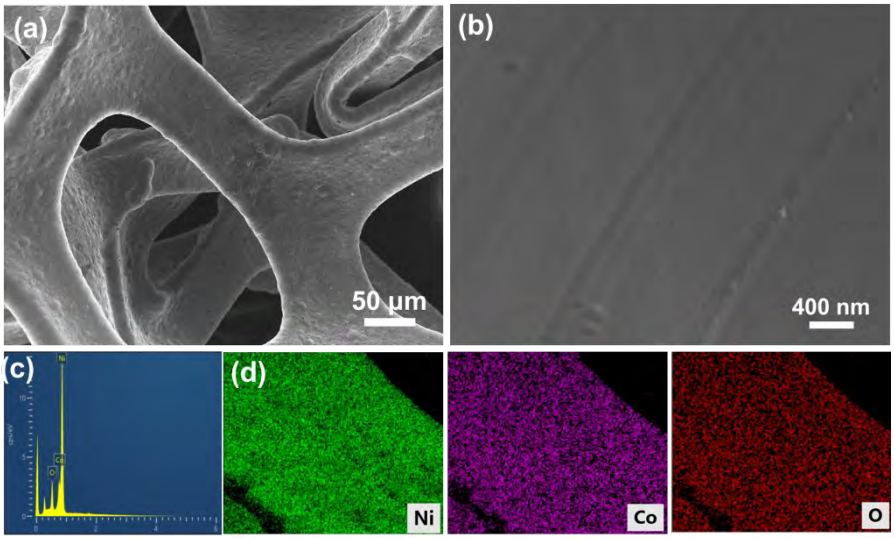

Figure S4. (a, b) SEM images of 12 nm CoO/NF, (c) EDX spectrum, (d) elemental maps.

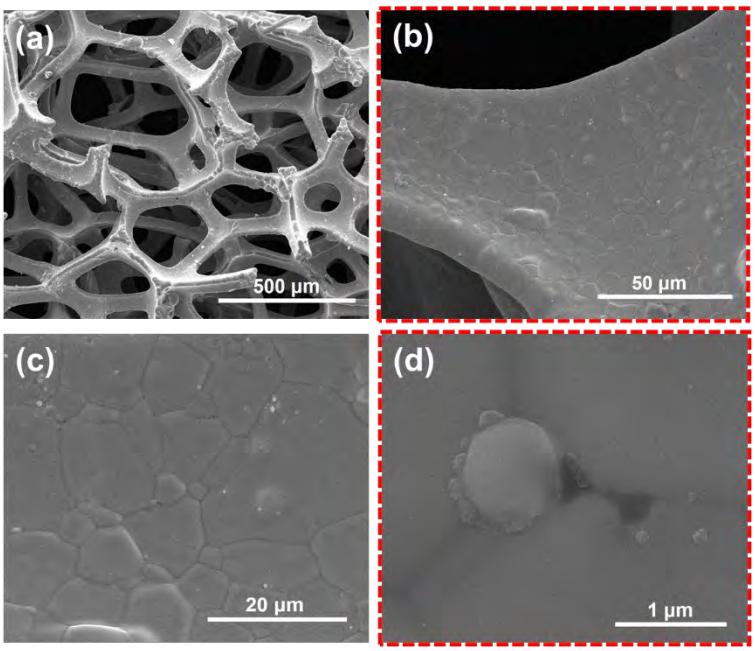

Figure S5. SEM images of Zr250/12CoO/NF.

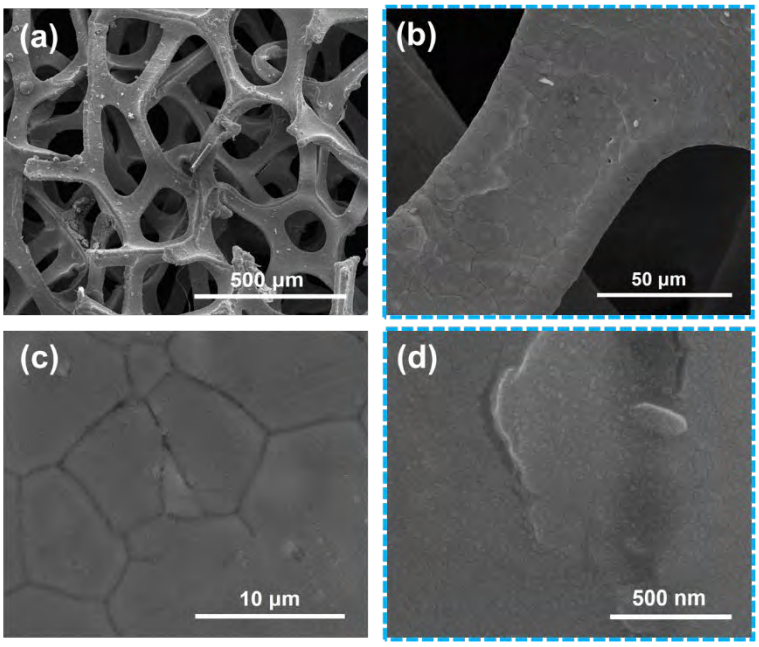

Figure S6. SEM images of Zr1000/12CoO/NF.

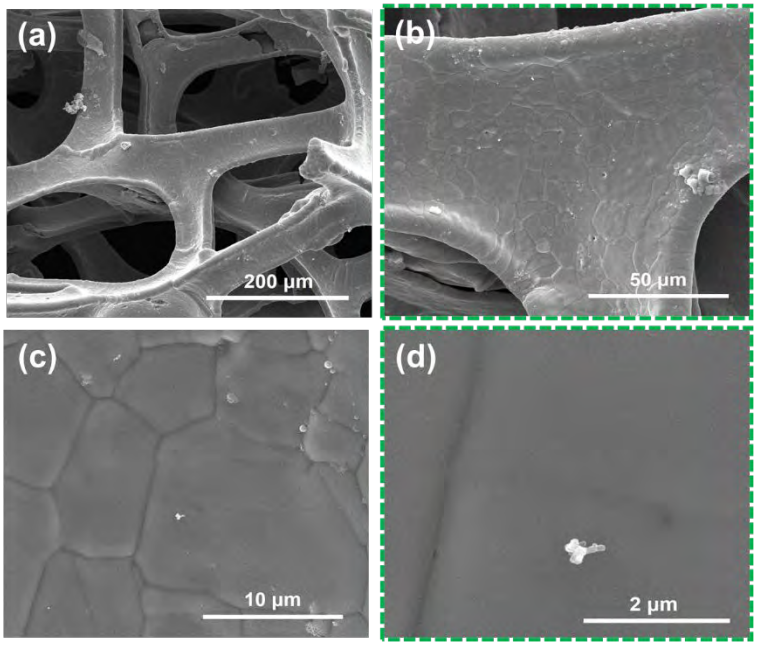

Figure S7. SEM images of Zr500/6CoO/NF.

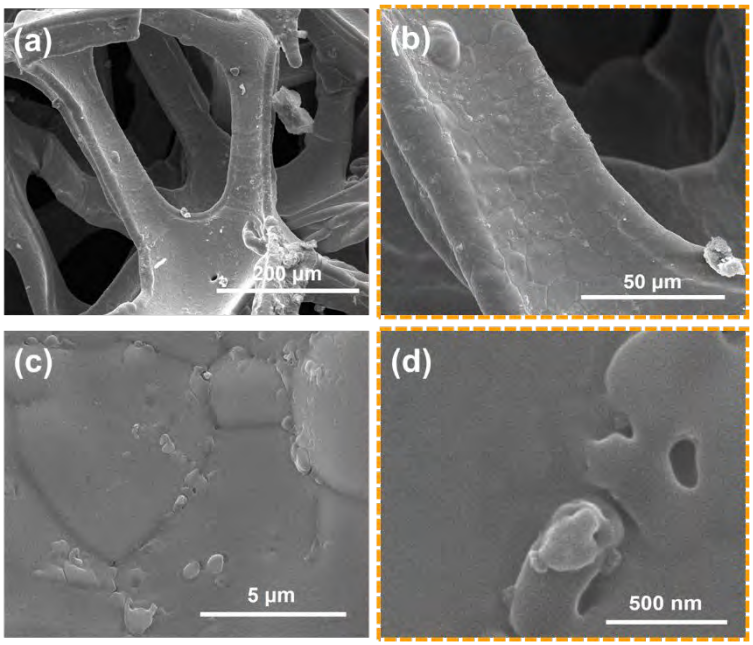

Figure S8. SEM images of Zr500/9CoO/NF.

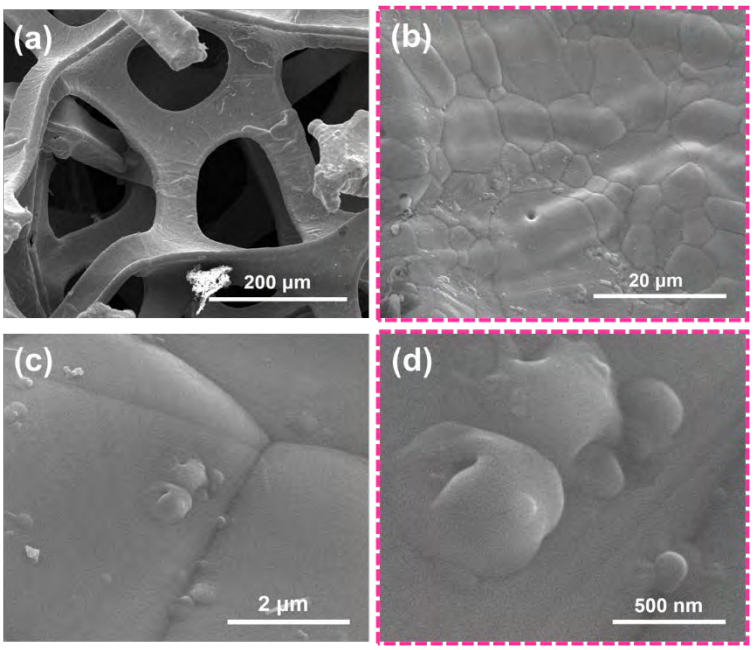

Figure S9. SEM images of Zr500/15CoO/NF.

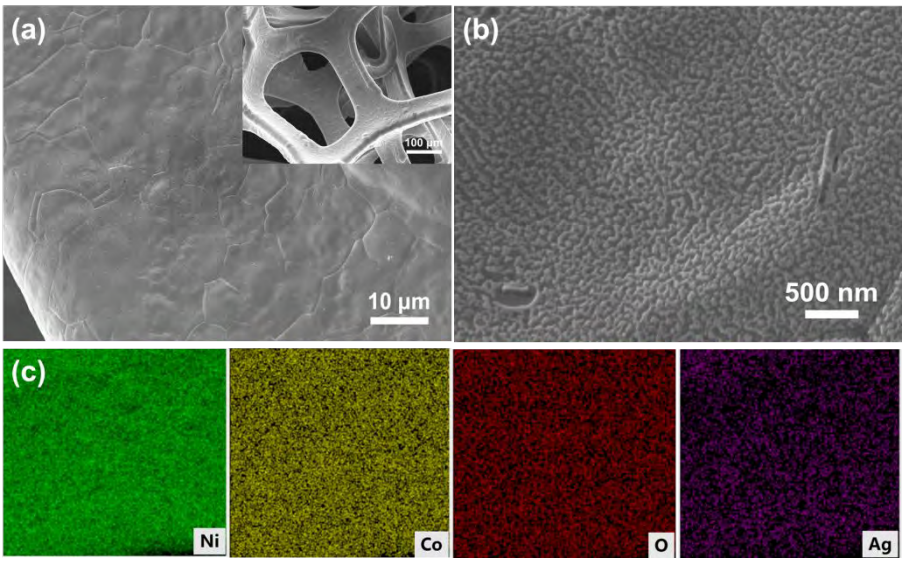

Figure S10. (a, b) SEM images of Ag500/12CoO/NF, (c) Elemental maps.

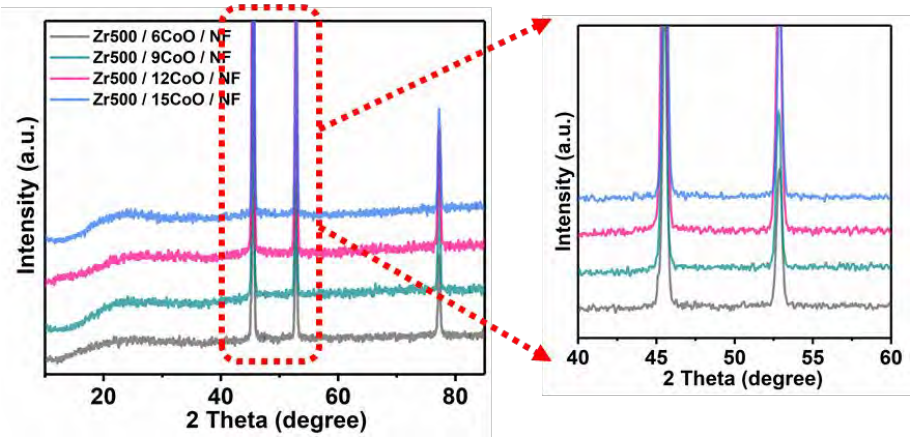

Figure S11. XRD pattern of Zr500/6CoO/NF, Zr500/9CoO/NF, Zr500/12CoO/NF, and Zr500/15CoO/NF.

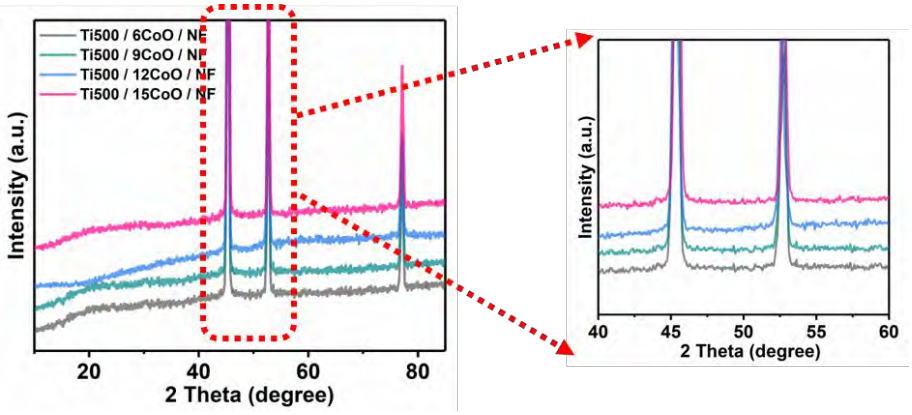

Figure S12. XRD pattern of Ti500/6CoO/NF, Ti500/9CoO/NF, Ti500/12CoO/NF, and Ti500/15CoO/NF.

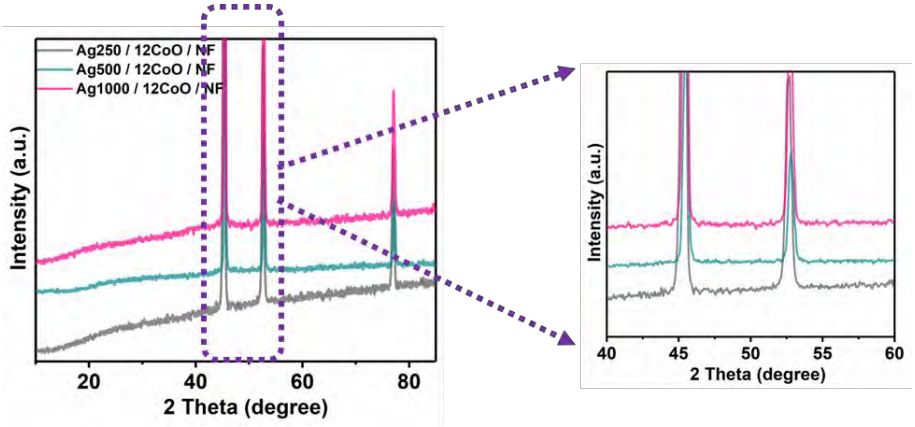

Figure S13. XRD pattern of Ag250/12CoO/NF, Ag500/12CoO/NF, and Ag1000/12CoO/NF.

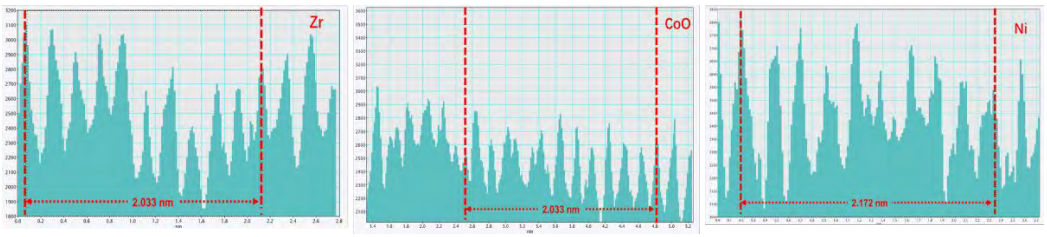

Figure S14 Lattice spacing distribution of Zr, CoO and Ni.

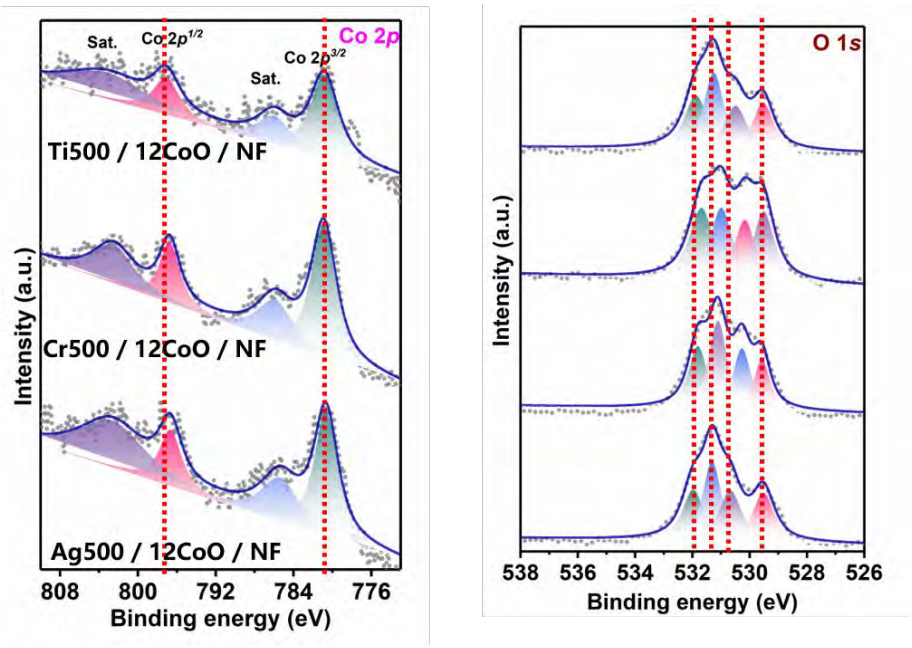

Figure S15. Co 2p and O 1s XPS spectra of Ti500/12CoO/NF, Cr500/12CoO/NF, and Ag500/12CoO/NF.

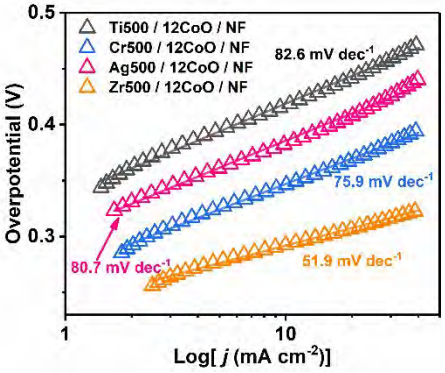

Figure S16. Tafel slopes of different catalysts.

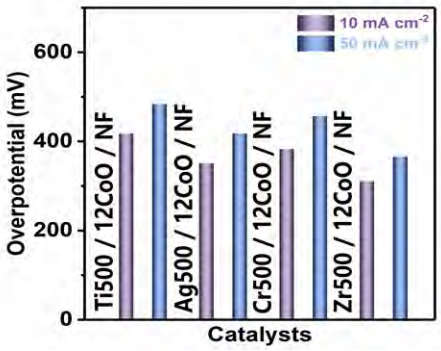

Figure S17. Overpotentials of different catalysts.

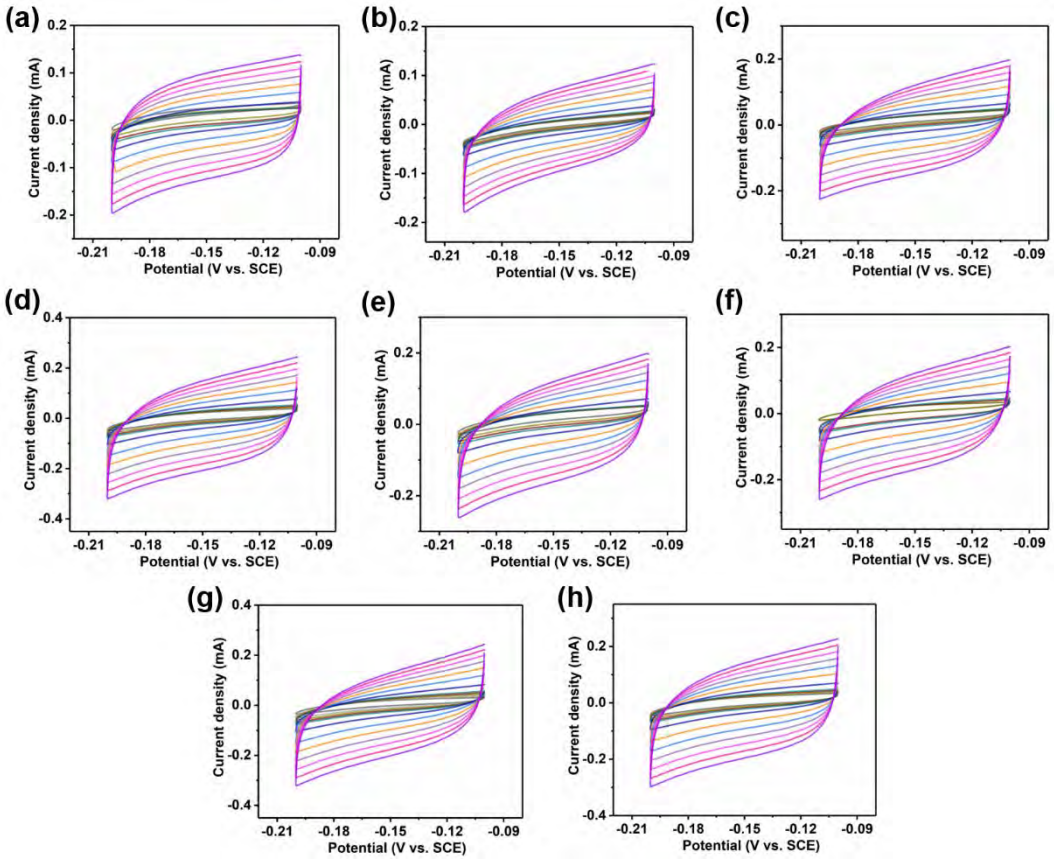

Figure S18. CV curve measured in the non-Faraday region.

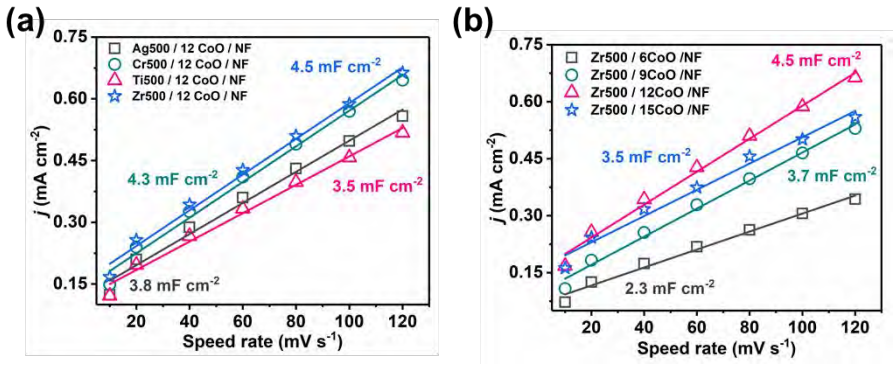

Figure S19 Plots of current density versus the speed rates: (a) Ag500/12CoO/NF, Cr500/12CoO/NF, Ti500/12CoO/NF, and Zr500/12CoO/NF; (b) Zr500/6CoO/NF, Zr500/9CoO/NF, Zr500/12CoO/NF, and Zr500/15CoO/NF.

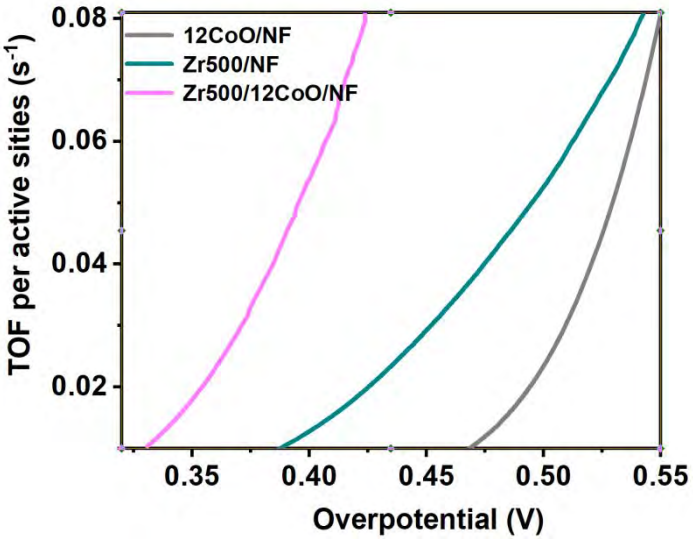

Fig.S20 TOF values for OER of 12 nm CoO/NF, Zr500/NF, and Zr500/12CoO/NF.

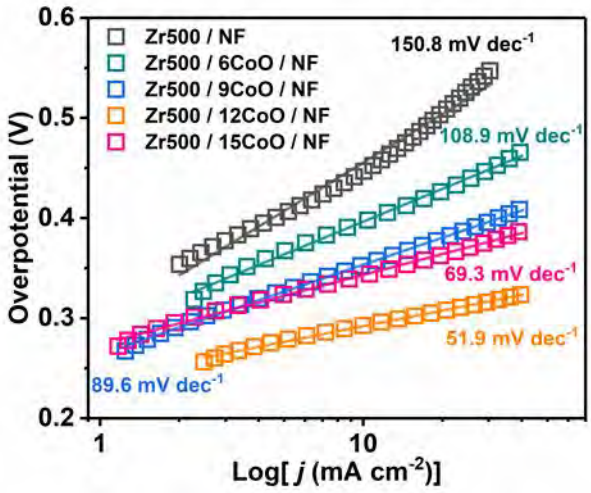

Figure S21. Tafel slopes of Zr500/NF, Zr500/6CoO/NF, Zr500/9CoO/NF, Zr500/12CoO/NF, and Zr500/15CoO/NF.

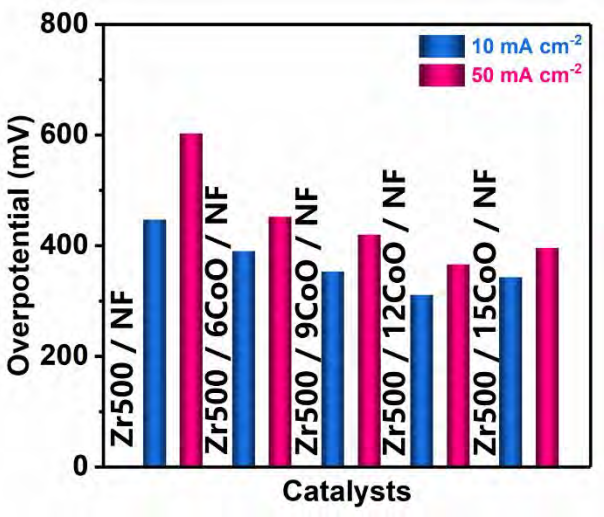

Figure S22. Corresponding overpotentials of Zr500/NF, Zr500/6CoO/NF, Zr500/9CoO/NF, Zr500/12CoO/NF, and Zr500/15CoO/NF.

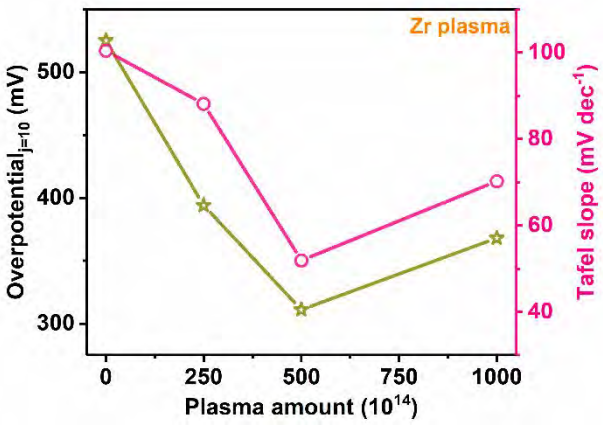

Figure S23. Variation trends of overpotential and Tafel slope with Zr plasma dose.

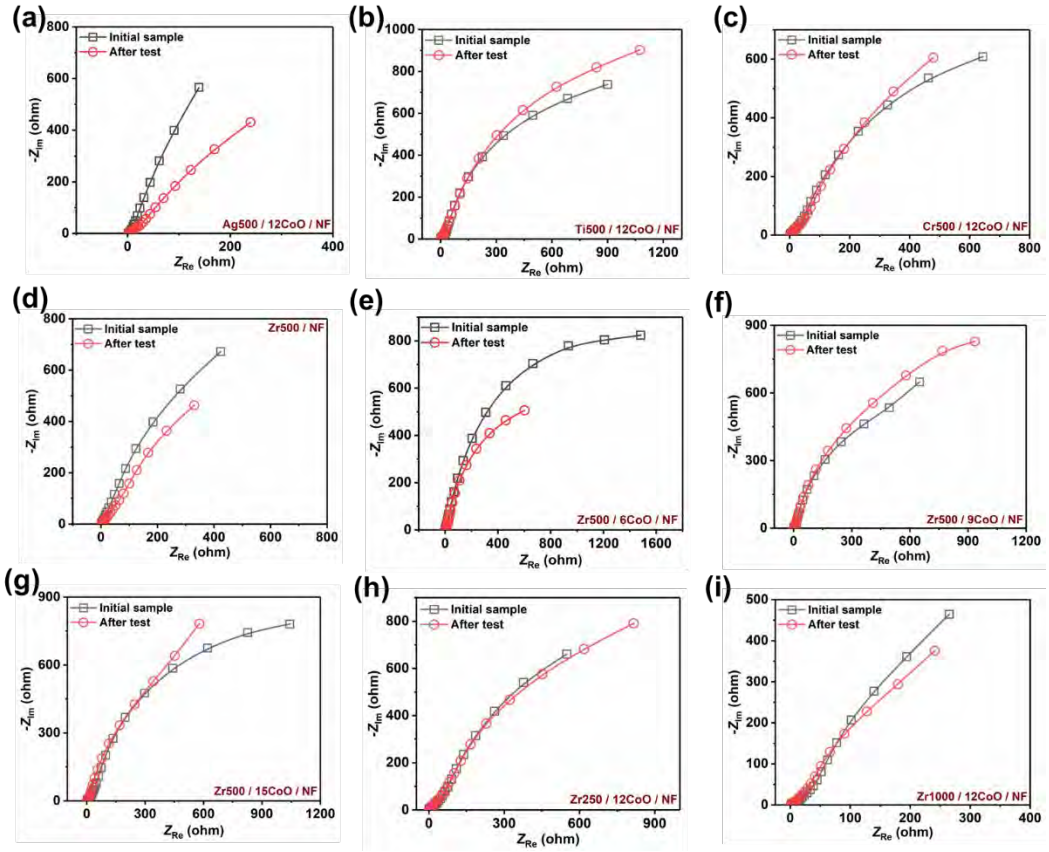

Figure S24. EIS measurement of different catalysts.

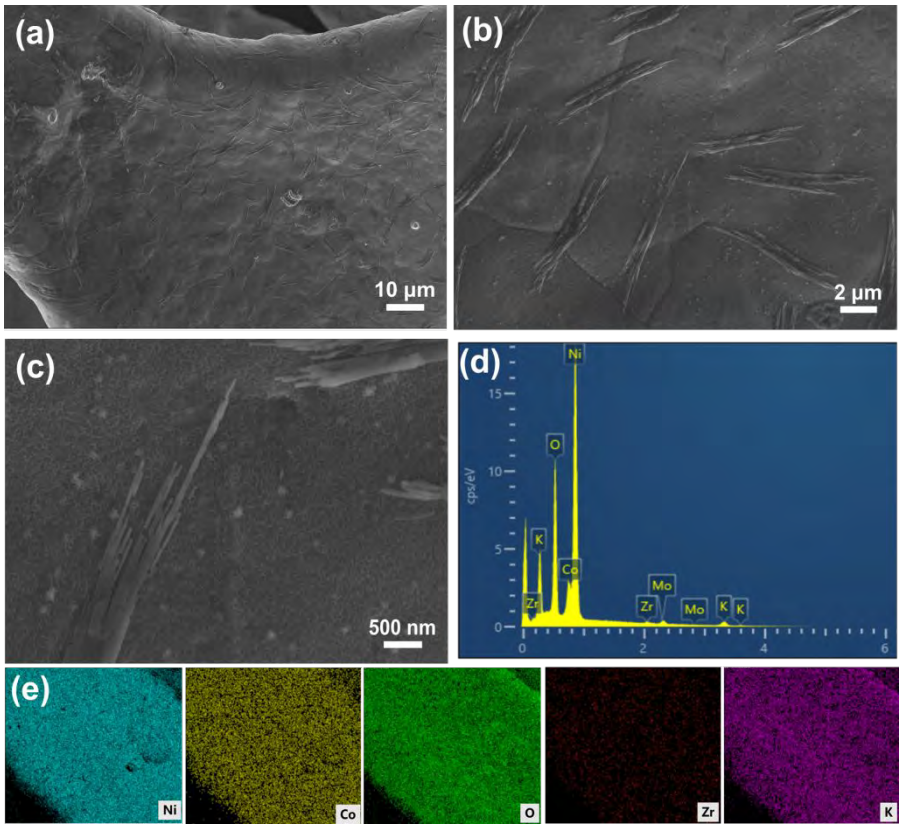

Figure S25. Zr500/12CoO/NF after long-term stability tests: (a-c) SEM images, (d) EDX, (e) Elemental maps.

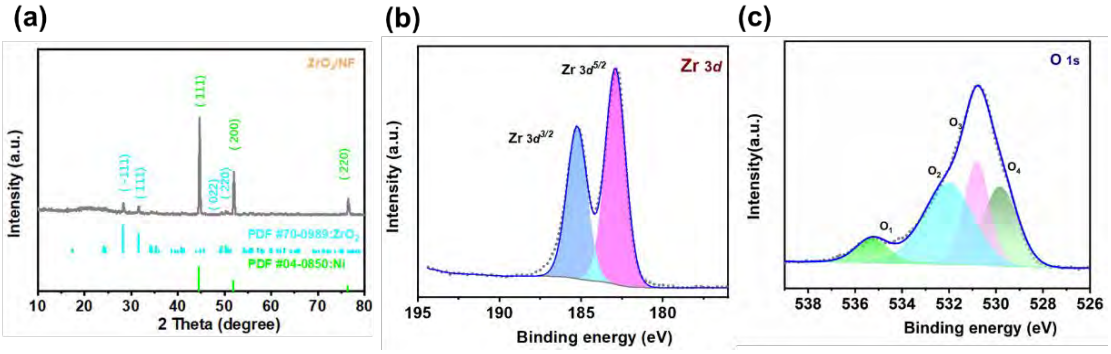

Figure S26 (a)XRD patterns of ZrO_2/NF; XPS spectra of ZrO_2/NF: (b)Zr 3d, and (c) O 1s

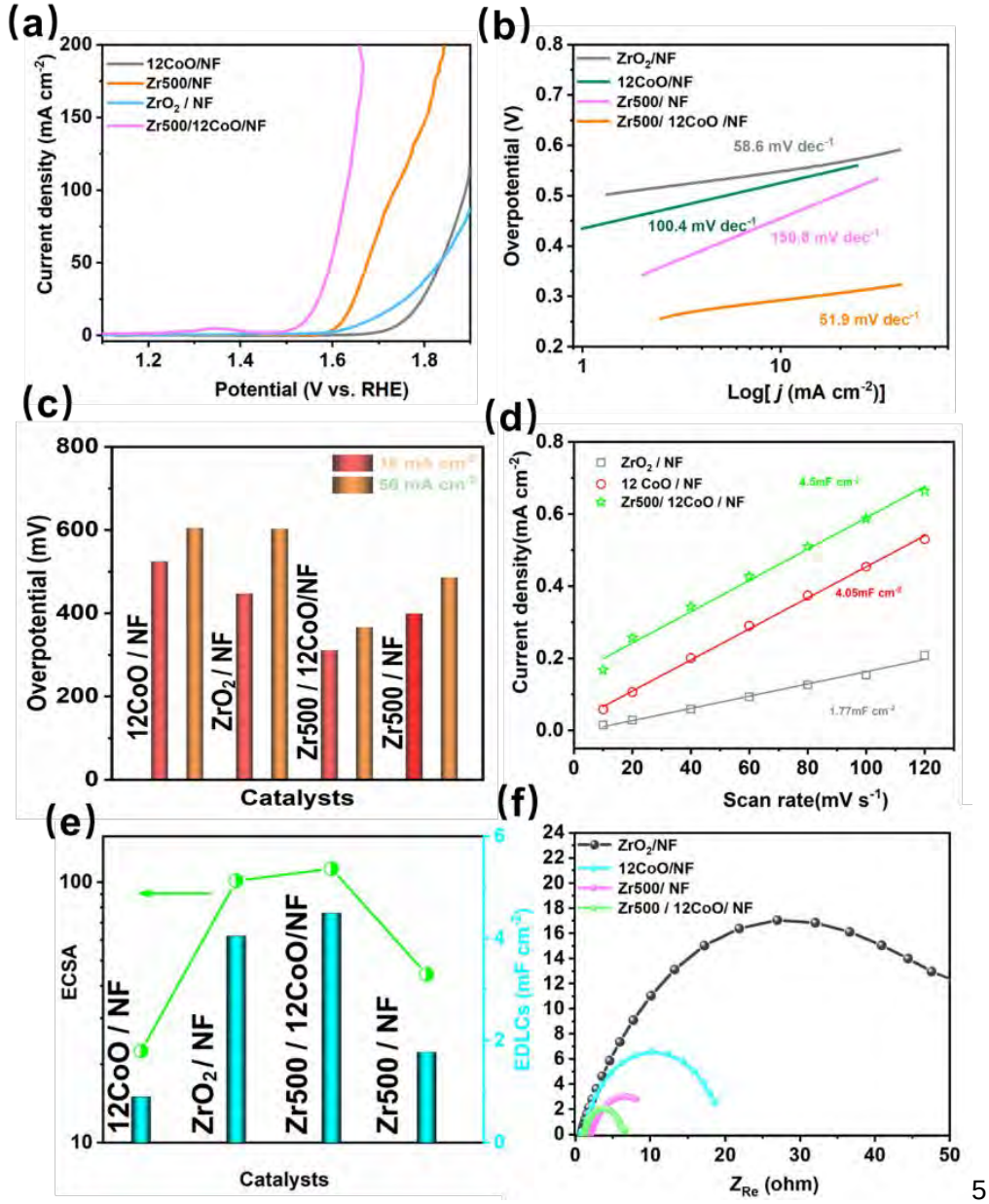

Figure S27 OER activity of 12CoO/NF, ZrO_2/NF, Zr500/NF, Zr500/12CoO/NF catalysts: (a) Polarization curves, (b) Tafel plots, (c) Overpotentials, (d) Plots of current density versus the speed rates, (e) EDLCs and ECSA results, (f) EIS measurement.

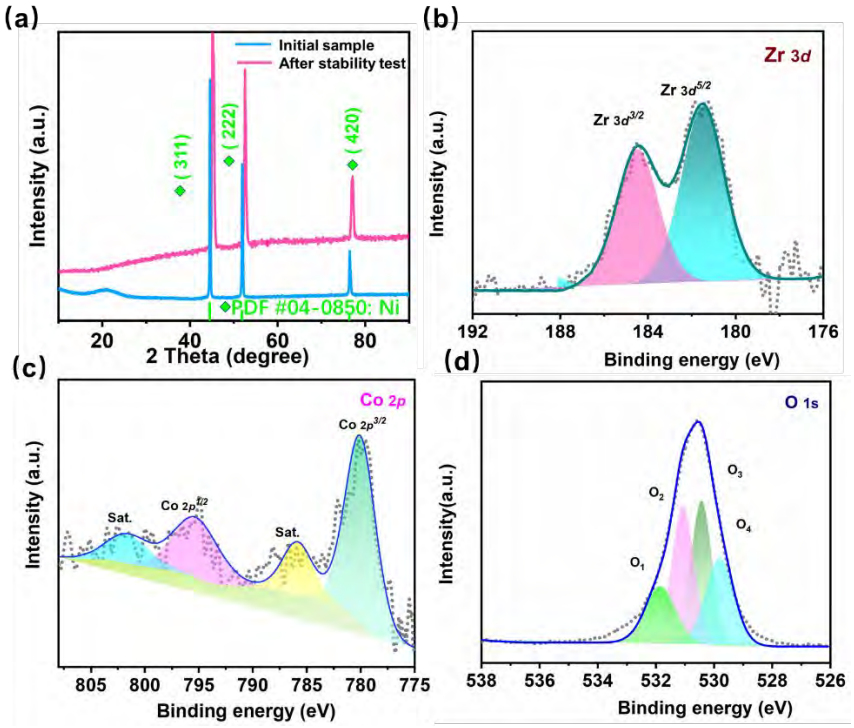

Figure S28 (a)XRD patterns of Zr500/12CoO/NF electrode before and after stability test; XPS spectra of Zr500/12CoO/NF: (b)Zr 3d, (c) Co2p and (d) O 1s.